JOURNAL OF GEOPHYSICAL RESEARCH, VOL. 91, NO. B14, PAGES 13,873–13,891, DECEMBER 10, 1986

Nature of the Magma Chamber Underlying the Mono Craters Area, Eastern California, as Determined From Teleseismic Travel Time Residuals

ULRICH ACHAUER,[1] LIZBETH GREENE, JOHN R. EVANS, AND H. M. IYER

U.S. Geological Survey, Menlo Park, California

A total of 94 teleseismic events of good quality were recorded by a dense mobile array of seismographs located in the Mono Craters volcanic area, eastern California, one of the youngest apparently active rhyolitic volcanic centers in North America. An inversion of travel time residuals from these events reveals a small anomalous volume, 200–600 km^3, directly beneath the Mono Craters with at least 7% low velocity and a top approximately 8–10 km deep. It reasonably may be interpreted as a magma chamber of molten or partially molten rock, although smaller, shallower, and differently placed than previously thought. The magma chamber probably is too small and young to produce a caldera-forming eruption within the foreseeable future.

INTRODUCTION

In recent years the analysis of teleseismic compressional waves has proven to be a useful tool for the detection of small anomalous velocity bodies in volcanic areas such as Long Valley, California [*Iyer and Stewart*, 1977; *Steeples and Iyer*, 1976], The Geysers–Clear Lake volcanic field [*Iyer et al.*, 1979; *Oppenheimer and Herkenhoff*, 1981], Mount Etna, Sicily [*Sharp et al.*, 1980], Coso geothermal area, California [*Reasenberg et al.*, 1980], Roosevelt Hot Springs, Utah [*Robinson and Iyer*, 1981], Newberry Volcano, Oregon (D. A. Stauber, unpublished manuscript, 1986) and other locations.

The Mono-Inyo Craters chain is a north trending silicic volcanic system extending from Long Valley caldera in the south to Mono Lake in the north (Figure 1). The chain is on the western margin of the Basin and Range province, just east of the Sierra Nevada range front. High heat flow, recent faulting, and strong seismic activity indicate that crustal extension still dominates the local tectonic regime, and that the region is volcanically and seismically active.

Kistler [1966] suggest that the Mono Craters erupted along the eastern part of a subcircular mylonitized Cretaceous pluton boundary. This mylonitized zone bounds the Grant Lake–June Lake embayment of the Sierra Nevada to the west and is inferred to underlie vents of the Mono Craters on the east (Figure 1). More recently, *Bailey and Koeppen* [1977] and *Bailey* [1982] mapped an additional series of concentric ring fractures east and south of the Mono Craters.

Bailey et al. [1976] and *Bailey* [1982] argue that together with these ring fracture systems, the youth, geochemistry, and frequency of eruptions suggest that the Mono Craters are fed by a ring dike from a moderately deep silicic magma chamber centered west of the craters beneath Pumice Valley. They infer that the chamber is largely molten and may still be rising toward the surface beneath an incipient caldera ring fracture zone (Figure 1). The teleseismic experiment described below is an attempt to test this model. While it tends to confirm the existence of a magma chamber, it suggests that the chamber is smaller and shallower than Bailey inferred and is located beneath the Mono Craters themselves rather than being centered beneath Pumice Valley.

DESCRIPTION OF EXPERIMENT

To investigate the crustal compressional velocity structure of the Mono Craters area a network of portable analog seismic recorders was installed for a period of 2 months during the summer of 1982. The network consisted of 16 stations with an average station spacing of about 6 km (Figure 1). These stations formed a 20 by 30 km grid centered near the Mono Craters.

The recording instruments used were 11 U.S. Geological Survey (USGS) analog FM "5-day recorders" [*Criley and Eaton*, 1978]. Two of the recorders also received data from a total of five radio transmitter sites. The transmitter sites each had one 1-Hz vertical seismometer, while the remaining stations included one vertical and two horizontal 1-Hz seismometers. Arrival times of *P* and *PKIKP* were read from the vertical component in each case.

During the 2-month recording period, 94 teleseismic events of good quality were recorded (Table 1 and Figure 2). All events were digitized and timed using digital band-pass filters and correlative methods similar to those of *Steeples and Iyer* [1976]. Timing precision is approximately 0.05 s. Theoretical travel times were calculated from hypocenters given in the "Preliminary Determinations of Epicenters," a U.S. Geological Survey periodical, and the *Herrin et al.* [1968] travel time tables. Absolute residuals then were obtained by subtracting the theoretical travel time from the observed travel time:

$$R_{ij} = T_{o_{ij}} - T_{th_{ij}} \tag{1}$$

To isolate the effects of local structure from the extraneous, but often larger, effects of source and path errors and anomalies, relative residuals were calculated. This correction was made by subtracting the weighted mean residual for each event from the absolute residuals of every station for that event:

$$RR_{ij} = R_{ij} - \frac{1}{\sum_{i=1}^{N_j} W_{ij}} \sum_{i=1}^{N_j} W_{ij} R_{ij} \tag{2}$$

[1] Now at Geophysikalisches Institut, Universität Fridericiana Karlsruhe, Karlsruhe, Federal Republic of Germany.

Paper number 6B6023.
0148-0227/86/006B-6023$05.00

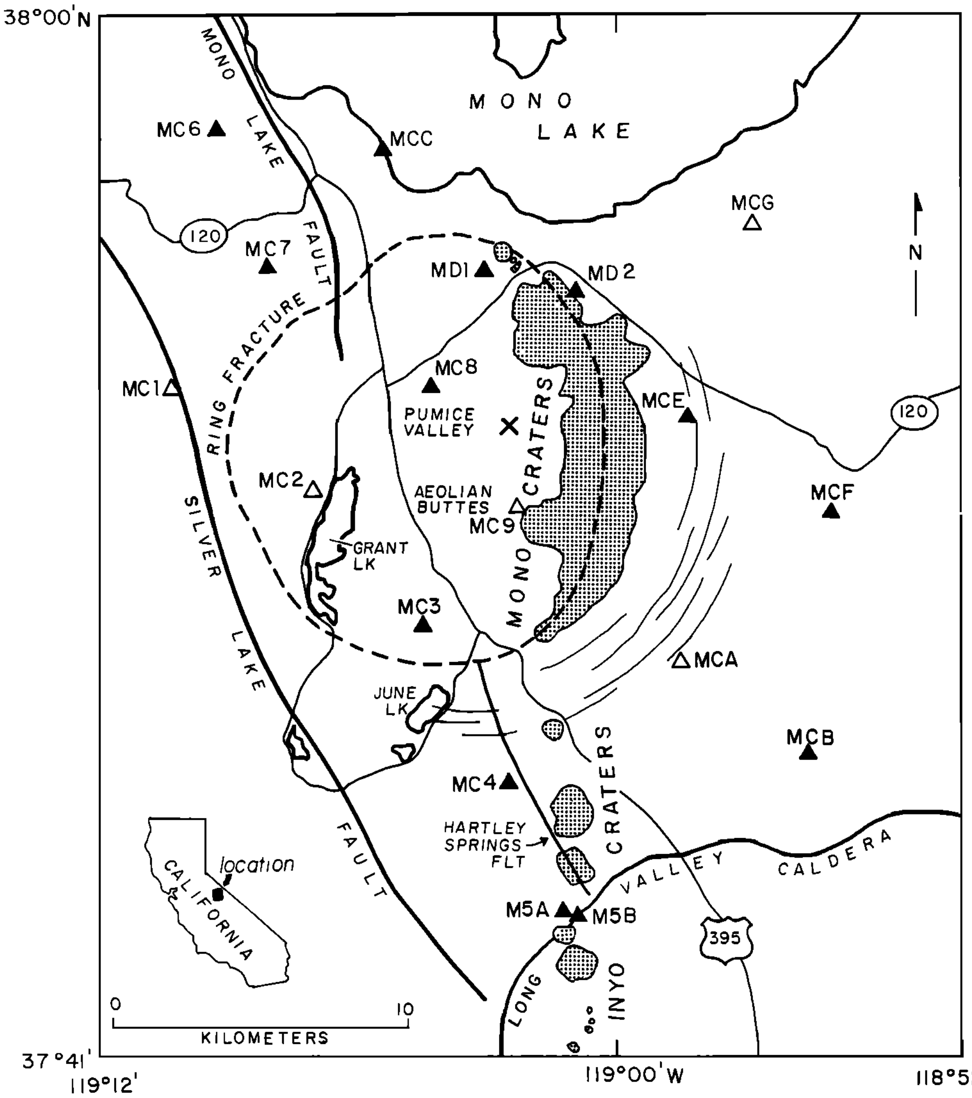

Fig. 1. Map of the Mono-Inyo Craters area showing major volcanic, tectonic, and geographic features, and the stations used in the teleseismic imaging experiment. Open symbols are transmitter sites; solid symbols are recorder sites. Cross north of MC9 is model center (cf. Figures 6a–6c). Geology based on work by *Kistler* [1966], *Bailey and Koeppen* [1977], and *Strand* [1967].

where i is the station index, j is the event index, N_j stations report event j, and W_{ij} are weights derived from subjective pick qualities. Relative residuals are used for the remainder of this paper and simply may be called "residuals."

Figure 3*a* shows mean relative residuals for each station with teleseisms arriving from all azimuths averaged together:

$$AR_i = \frac{1}{M_i} \sum_{j=1}^{M_i} RR_{ij} \tag{3}$$

where M_i events were recorded at station i during the experiment. These average residuals are independent of azimuth and incidence angle and reflect velocity heterogeneities at shallow depth. They are called the "invariant" part of the residuals.

Equation (3) is subject to an azimuthal bias caused by the inhomogeneous distribution of events around the earth. For comparison, we calculated unbiased invariant residuals by weighting the residuals so that each way "bundle," discussed below, contributed equally to the invariant residual. The azimuthal bias revealed by this procedure is very small, generally less than 0.02 s. It has no significant effect on the following discussion and no effect at all on the inversion results presented later.

To show the effects of deeper structures, the teleseismic compressional waves next were divided into five groups according to ray orientation beneath the array. All events in such a ray bundle are averaged together and the invariant part is removed according to

$$DR_{ib} = \left[\frac{1}{X_{ib}} \sum_{j=1}^{X_{ib}} RR_{ijb} \right] - AR_i \tag{4}$$

where X_{ib} is the number of events reported at station i for ray bundle b. P waves have incidence angles from about 14°–30° near the surface and are divided into four groups according to azimuth (Figure 3*b*–3*e*). The azimuth groupings chosen follow the natural clustering of events to the northwest, southeast, and southwest, as seen from the western United States. The fifth ray group (Figure 3*f*) is *PKIKP* with all azimuths grouped together; incidence angles are less than 6° for *PKIKP*. The changes in residual patterns between these five ray directions are due to anomalous velocity regions at depth

TABLE 1. Hypocenters of Teleseismic Events Used

Location	Date	Origin Time	Depth, km	M_b	Latitude N	Longitude W
El Salvador	June 19, 1982	0621:58.0	82	6.2	13°18.8′	89°20.3′
Fiji Islands	June 19, 1982	1849:02.5	611	4.9	−21°04.2′	178°46.6′
Vanuatu Islands	June 19, 1982	2246:08.8	33	5.6	−14°43.1′	−167°52.6′
North Atlantic	June 20, 1982	0829:15.3	10	5.1	30°42.0′	41°44.0′
El Salvador	June 21, 1982	0530:28.7	61	4.9	13°03.6′	89°19.7′
Santa Cruz Islands	June 21, 1982	1915:56.3	48	5.6	−10°47.0′	−164°10.4′
Banda Sea	June 22, 1982	0418:40.5	450	6.3	−7°20.3′	−126°02.6′
Aleutian Islands	June 22, 1982	0705:27.1	90	4.8	53°55.7′	166°38.6′
Honshu, Japan	June 23, 1982	0151:54 8	476	5.3	29°03.7′	−138°46.1′
Fiji Islands	June 23, 1982	1324:09.3	623	4.8	−20°45.0′	178°53.1′
South Atlantic*	June 24, 1982	0916:44 3	10	5.6	−44°00.5′	15°58.7′
Sumatera	June 25, 1982	1023:51.2	35	5.3	−6°21.4′	−103°26.2′
Kuril Islands*	June 30, 1982	0157:34.1	33	6.6	44°40.7′	−151°08.6′
Chile	July 1, 1982	0256:27.2	149	5.0	−18°40.8′	69°23.8′
Aleutian Islands	July 1, 1982	0741:53.2	48	6.3	51°25.6′	179°56.6′
Chile-Bolivia	July 1, 1982	0847:32.7	119	4.4	−21°25.8′	68°48.0′
Tuamotu Arch.	July 1, 1982	1701:58.8	1	5.2	−21°46.0′	139°03.0′
El Salvador	July 2, 1982	1159:35.6	64	5.0	13°03.4′	89°17.2′
Volcano Islands	July 3, 1982	1436:30.3	165	5.2	22°19.0′	−143°24.7′
Kazakh, SSR	July 4, 1982	0117:14.4	1	6.1	49°59.7′	−78°51.4′
Ryukyu Island	July 4, 1982	0120:06.8	536	6.3	27°55.7′	−136°58.0′
Colombia	July 4, 1982	0616:08.4	54	5.5	7°39.2′	72°11.8′
Japan	July 5, 1982	0856:55.6	116	5.7	30°59.8′	−130°27.1′
Fiji Islands	July 5, 1982	2122:26.9	615	5.5	−20°49.7′	178°48.1′
Peru	July 11, 1982	0213:37.7	39	5.3	−16°38.9′	73°12.8′
North Atlantic	July 11, 1982	1040:12.4	10	5.1	23°43.6′	44°53.9′
Honshu, Japan	July 13, 1982	0845:55.7	341	4.9	32°56.3′	−137°39.2′
Gilbert Islands	July 13, 1982	1349:48.3	30	5.5	−3°18.3′	−177°35.5′
Japan	July 14, 1982	1042:13.5	325	5.3	45°38.5′	−143°21.8′
Alaska	July 14, 1982	1215:47.6	157	5.0	60°30.8′	153°40.2′
Gilbert Islands	July 15, 1982	0213:49.3	33	5.6	−3°20.5′	−177°34.9′
Fiji Islands	July 16, 1982	1433:40.7	547	5.4	−21°24.7′	178°50.2′
Gilbert Islands	July 17, 1982	1832:09.7	33	5.4	−3°15.0′	−177°37.1′
Vanuatu Islands	July 17, 1982	2202:07.9	37	5.6	−21°44.1′	−173°07.9′
Colombia	July 17, 1982	2224:14.2	163	4.9	6°47.5′	73°02.5′
Argentina	July 19, 1982	2352:55.2	207	5.2	−23°56.9′	66°44.3′
Kamchatka	July 20, 1982	1511:47 3	32	5.5	54°33.0′	−161°28.3′
Peru	July 21, 1982	2211:03.5	99	5.1	−13°12.9′	75°05.6′
Honshu, Japan	July 23, 1982	1125:01.3	32	5.1	36°07.3′	−141°45.5′
Java	July 23, 1982	1351:42 3	34	5.2	−10°47.8′	−111°42.9′
Honshu, Japan	July 23, 1982	1423:53 5	37	6.2	36°11.6′	−141°42.1′
Honshu, Japan*	July 23, 1982	1505·07 8	50	5.1	36°09.4′	−141°43.6′
Honshu, Japan	July 23, 1982	1754·02 4	31	5.7	36°04.0′	−141°43.5′
Africa	July 24, 1982	0917:27.5	10	5.2	−52°52.8′	−20°51.7′
New Britain	July 24, 1982	1233:56.2	76	4.6	−5°51.7′	−151°17.0′
Aleutian Islands*	July 25, 1982	0539:01.8	106	4.5	52°02.4′	−178°26.6′
Honshu, Japan	July 25, 1982	0801:28.6	45	5.5	36°18.8′	−141°38.6′
Tuamotu Arch.	July 25, 1982	1801:58 1	1	5.6	−21°51.8′	138°56.6′
Africa	July 26, 1982	0343:24 0	10	5.0	−52°48.2′	−20°56.6′
El Salvador	July 26, 1982	1034:58.6	67	5.1	13°21.9′	89°03.8′
Galapagos Islands	July 27, 1982	1127:17.9	10	5.2	1°15.2′	90°41.8′
Aleutian Islands	July 27, 1982	1234·51 8	228	4.6	52°50.4′	176°24.6′
Tonga Islands	July 30, 1982	0340:51.4	33	5.7	−18°39.1′	173°38.1′
Aleutian Islands	July 31, 1982	0629:15.5	38	6.2	51°45.3′	−176°08.2′
Tonga Islands	Aug. 2, 1982	1100:07.0	33	4.9	−20°21.1′	174°27.2′
Mariana Islands*	Aug. 3, 1982	0604:39.6	47	5.8	13°44.5′	−146°20.4′
New Guinea	Aug. 5, 1982	0728:08.8	113	5.6	−5°46.0′	−146°34.0′
Chile	Aug. 5, 1982	0815:01.7	33	5.0	−37°37.7′	73°00.7′
Chile	Aug. 5, 1982	0916:41.3	40	5.4	−26°40.7′	70°39.4′
Gilbert Islands	Aug. 5, 1982	1524:23.1	33	5.2	−3°22.8′	−177°39.7′
Santa Cruz Islands	Aug. 5, 1982	2032:52.9	31	6.2	−12°35.8′	−165°55.9′
Aleutian Islands	Aug. 6, 1982	0453:58.6	64	5.4	51°56.8′	176°05.1′
Indian Rise	Aug. 6, 1982	1345:26.8	10	5.1	−10°22.7′	−66°14.9′
Fiji Islands	Aug. 7, 1982	0120:29.5	33	5.1	−16°14.0′	−178°17.0′
Tonga Islands*	Aug. 7, 1982	1309:21.5	33	5.0	−24°26.7′	175°12.7′
Samoa	Aug. 7, 1982	1820:22.1	33	5.5	−16°32.9′	172°38.2′
Alaska	Aug. 7, 1982	1953:46.1	15	4.8	65°59.9′	166°46.0′
Bali	Aug. 7, 1982	2056:22.7	33	6.1	−11°08.6′	−115°25.1′
Kamchatka	Aug. 8, 1982	0614:09.5	140	5.3	51°03.1′	−156°26.4′
Peru	Aug. 9, 1982	0450:38.6	164	4.8	−15°13.8′	71°02.5′
New Britain	Aug. 9, 1982	0502:34.4	163	5.4	−4°38.5′	−151°45.8′
New Britain	Aug. 9, 1982	0933:25.3	195	5.0	−4°59.7′	−151°04.9′
New Britain	Aug. 9, 1982	1847:03.8	143	5.3	−4°58.9′	−151°22.3′

TABLE 1. (continued)

Location	Date	Origin Time	Depth, km	M_b	Latitude N	Longitude W
Vanuatu Islands	Aug. 9, 1982	2327:31.9	229	5.0	−18°47.1′	−169°10.3′
Peru	Aug. 10, 1982	0451:48.5	33	5.5	−5°21.1′	77°22.0′
Tonga Islands	Aug. 11, 1982	0808:50.1	33	5.1	−19°28.9′	173°02.0′
Samoa	Aug. 11, 1982	1202:02.8	33	5.3	−16°25.4′	172°42.2′
Honshu, Japan	Aug. 12, 1982	0433:00.1	34	5.3	34°53.9′	−139°29.0′
Gilbert Islands	Aug. 12, 1982	1003:15.5	33	5.5	−3°23.2′	−177°34.1′
Honshu, Japan	Aug. 12, 1982	1146:50.8	33	5.3	39°24.4′	−143°16.6′
Gilbert Islands	Aug. 13, 1982	0605:45.1	33	5.3	−3°18.1′	−177°35.8′
Mariana Islands	Aug. 14, 1982	0058:54.0	156	5.3	18°29.2′	−145°52.0′
New Guinea	Aug. 14, 1982	1427:40.2	106	5.9	−5°03.3′	−143°57.8′
Peru	Aug. 15, 1982	0611:15.9	106	5.5	−10°03.8′	76°21.1′
Honshu, Japan	Aug. 15, 1982	1658:15.8	50	5.4	36°29.8′	−141°02.0′
Guatemala	Aug. 16, 1982	0632:58.8	76	5.0	14°22.5′	91°36.2′
Fiji Islands	Aug. 16, 1982	0721:26.9	596	5.1	−19°42.5′	178°08.6′
Aleutian Islands	Aug. 16, 1982	2058:20.7	49	5.4	51°47.0′	174°03.4′
Kuril Islands	Aug. 17, 1982	0528:59.2	48	5.0	45°41.3′	−151°21.2′
Solomon Islands	Aug. 17, 1982	2255:46.9	33	5.4	−9°15.0′	−157°39.7′
Mexico†	Aug. 18, 1982	0358:20.8	38	5.0	18°04.2′	105°34.6′
Vanuatu Islands	Aug. 19, 1982	0440:48.2	39	5.6	−19°04.0′	−169°34.7′
Panama	Aug. 19, 1982	1559:01.5	10	6.2	6°43.1′	82°40.8′
Gilbert Islands	Aug. 19, 1982	1633:25.6	33	5.1	−3°25.1′	−177°40.3′

*Too few readings; not used in ACH inversion.
†Not used in Figure 3.

beneath the array. These patterns usefully can be thought of as the "shadows" of deep objects projected to the surface along five different illuminating "beams."

OBSERVATIONS

The invariant part of the delay pattern (Figure 3*a*) shows that the stations near Mono Lake (MCC, MD1, MD2, and MCG) are 0.1–0.2 s late. These delays probably are caused by low-velocity sediment filling Mono basin, *Pakiser*'s [1976] time terms form a very similar delay pattern which he related to a thin layer of very low-velocity sediments filling the basin.

This invariant part has been subtracted from Figures 3*b*–3*f*, so that the Mono basin sediment effect is removed in these maps. The remaining part reveals a deeper low-velocity anomaly. A delayed region migrates with event azimuth and appears at stations MCA and MCB for northwest *P* wave events (Figure 3*e*); MC2, MC3, and MC9 for northeast events (Figure 3*b*); MC7, MC8, and MD1 for southeast events

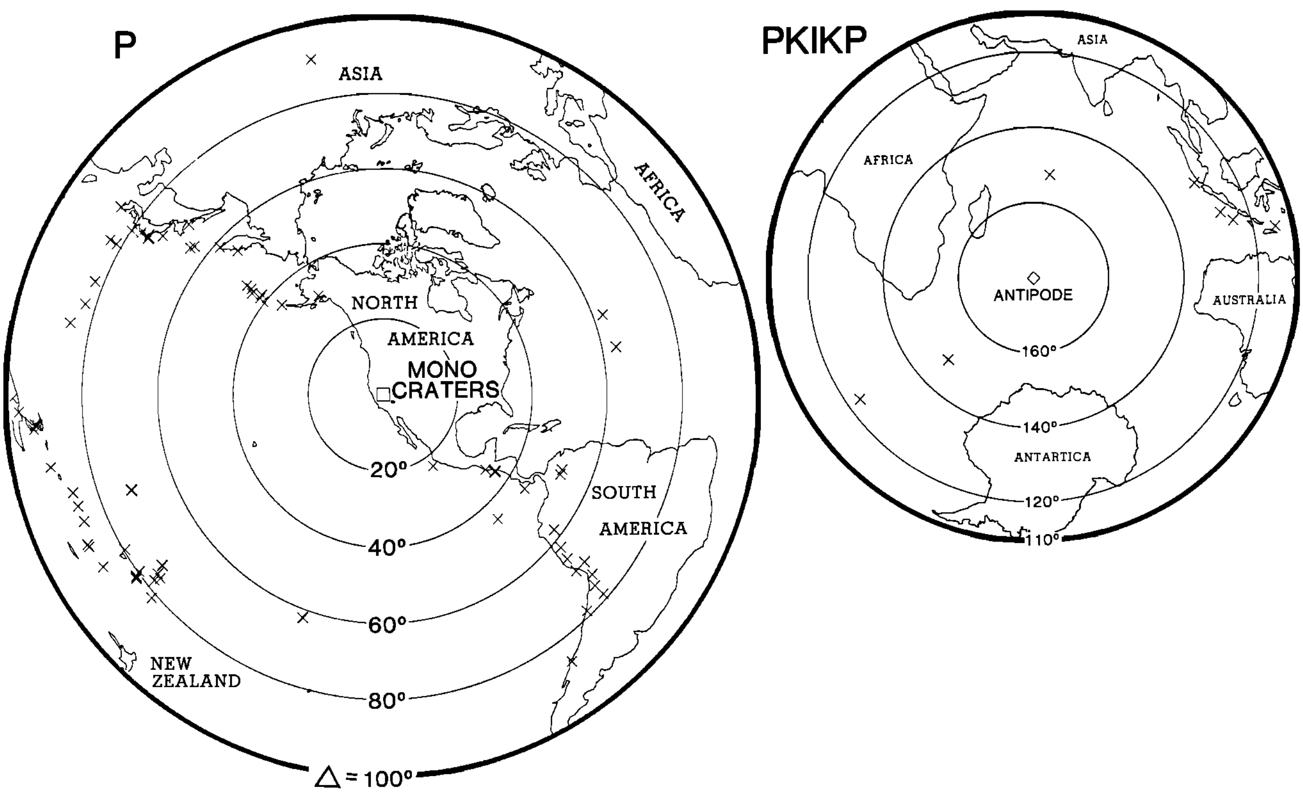

Fig. 2. Azimuthal equidistant maps of epicenters (crosses) of teleseismic events used in this study. The Mono Craters area is indicated by the square (*P* events); the antipode of the area is indicated by the diamond (*PKIKP* events). Hypocenter data are listed in Table 1

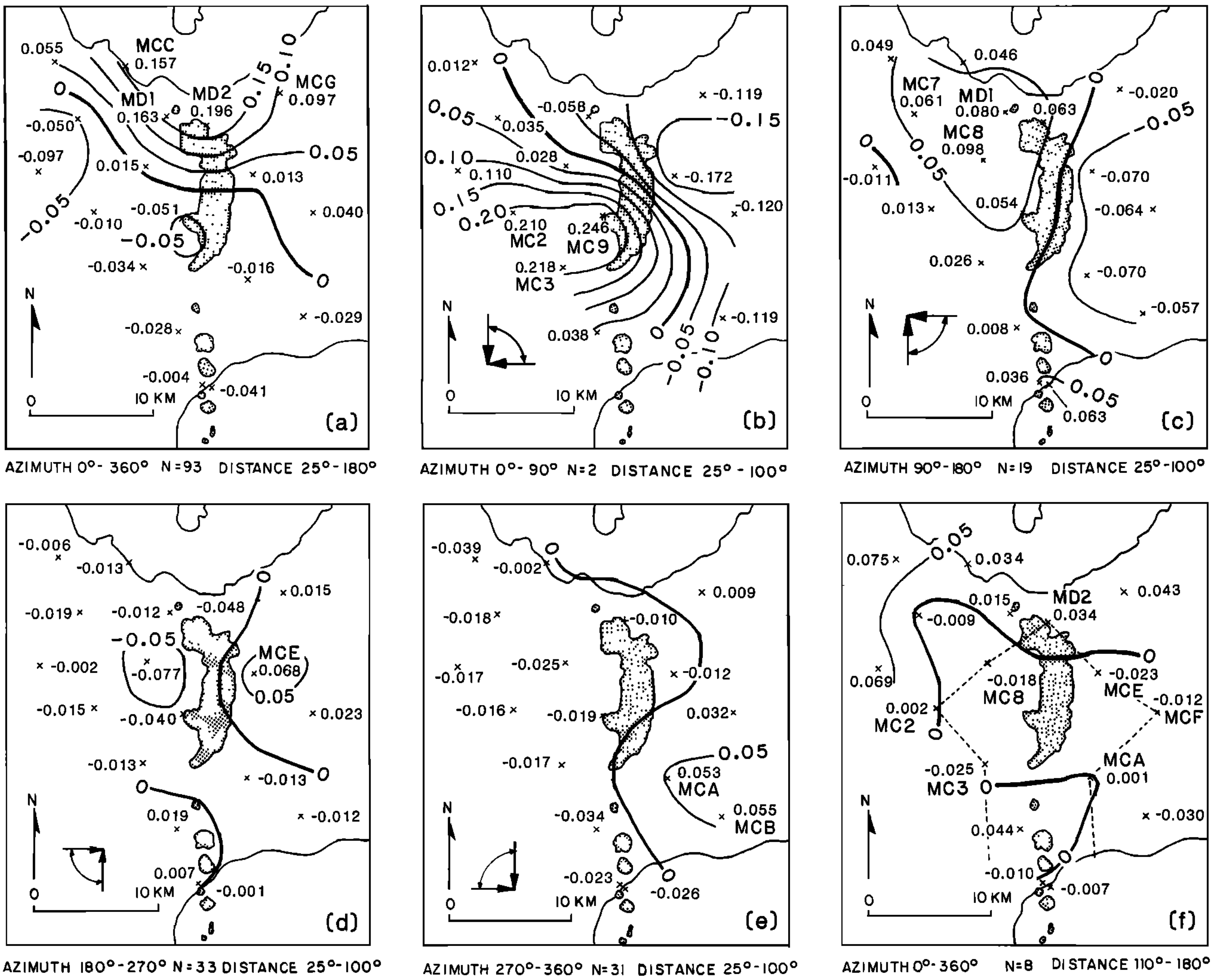

Fig. 3. Mean relative residuals for six distance-azimuth groups (seconds; positive indicates delays). (*a*) All events together (i.e., "invariant part"); (*b*) northeast *P* wave events; (*c*) southeast events; (*d*) southwest events; (*e*) northwest events; and (*f*) *PKIKP*. Dotted line in Figure 3*f* shows approximate maximum size of the low-velocity feature. Invariant part has been removed from Figures 3*b*–3*f*. "*N*" is the number of events per group (not all stations report for each event).

(Figure 3*c*); and MCE for southwest events (Figure 3*d*). In each case a small region of delayed arrivals is seen near the Mono Craters and is always on the opposite side of the craters from the events.

These delays (comparing opposite sides of the craters along single ray corridors) average about 0.2 s for the four main ray bundles (Figures 3*b*–3*e*). The northeast quadrant (Figure 3*b*) contributes strongly to this average but contains only two

TABLE 2*a*. Inversion Models

	Model A			Model B			Model C		
Layer	Thickness, km	Horizontal Block Size, km × km	Initial Velocity, km/s	Thickness, km	Horizontal Block Size, km × km	Initial Velocity, km/s	Thickness, km	Horizontal Block Size, km × km	Initial Velocity, km/s
1	*	special	4.5	*	special	†		special	†
2	7.5	5 × 5	6.0	7.5	5 × 5	6.0	9.0	6 × 6	6.0
3	7.5	5 × 5	6.25	7.5	5 × 5	6.25	9.0	6 × 6	6.25
4	7.5	5 × 5	6.5	7.5	5 × 5	6.5	9.0	6 × 6	6.5
5	7.5	5 × 5	6.9	7.5	5 × 5	6.9	9.0	6 × 6	6.9

Description	Model A	Model B	Model C
Block orientation‡	45° × 135°	45° × 135°	45° × 135°
Damping, $s^2/\%^2$	0.0010	0.0010	0.0005
Data variance, s^2	0.0170	0.0088	0.0088
Remaining variance, s^2	0.0045	0.0036	0.0033
Variance reduction, %	73	60	62

*Layer thickness equals the station elevation; bottom of first layer is at sea level.
†See Table 2*b* for velocities.
‡Azimuth of block edges

TABLE 2b. Station Coordinates and Sediment-Corrected Velocities for Layer 1

Station	Latitude N	Longitude W	Elevation, m	Velocity, km/s
MC1	37°53.13′	119°10.18′	2640	5.40
MC2	37°51.28′	119°07.06′	2323	4.50
MC3	37°48.86′	119°04.44′	2354	4.50
MC4	37°46.01′	119°02.48′	2692	4.95
M5A*	37°43.64′	119°01.21′	2561	4.50
M5B*	37°43.56′	119°00.95′	2442	4.50
MC6	37°57.96′	119°09.24′	2847	4.72
MC7	37°55.40′	119°08.03′	2296	4.95
MC8	37°53.26′	119°04.25′	2091	4.50
MC9	37°51.04′	119°02.19′	2244	4.50
MCA	37°48.25′	118°58.58′	2497	4.95
MCB	37°46.59′	118°55.55′	2341	4.50
MCC	37°57.66′	119°05.36′	1963	3.38
MD1†	37°55.49′	119°03.03′	2073	3.83
MD2†	37°55.08′	119°00.91′	2064	3.38
MCE	37°52.81′	118°58.31′	2262	4.95
MCF	37°51.11′	118°55.02′	2540	4.72
MCG	37°56.37′	118°56.85′	2037	3.60

*M5A moved to M5B; July 4, 1982.
†MD1 moved to MD2; June 27–29, 1982.

events and may be less accurate than the other three; the mean contrast in the three remaining quadrants is 0.13 s.

Though small, this contrast is significant. The standard deviations of the means plotted in Figure 3 are about 0.01 s, and the several means used together to make such comparisons give a combined accuracy of about ±0.05 s. The observed 0.13-s contrast is about 3 times larger than this error estimate.

This moving pattern of delays can be explained most easily by a small midcrustal low-velocity region beneath the Mono Craters. The horizontal dimension of the delaying volume is about 1 or 2 times the distance between stations (since the delays cover one to three stations) or about 6–12 km. Assuming, for example, a 10-km-diameter sphere causing a maximum of 0.2-s delay, as discussed above, one can estimate that it would have about 11% low velocity if embedded in a 6 km/s layer. The Mono Craters low-velocity feature is of this order.

The depth of the feature can be estimated from the ray incidence angles and the distance the delay shadow moves between opposite azimuths. In this case the low-velocity region must be centered at roughly 12–20 km deep. Based on the positions of the residual maxima and the ray azimuths used, it is probably beneath the southern half of the Mono Craters.

The fifth (near-vertical) ray bundle (Figure 3*f*) unfortunately lacks any data above this suspect region. In fact, the near-zero residuals at MC2, MC3, MC8, MCA, MD2, MCE, and MCF constrain the horizontal size and position of the anomalous volume to be within the dashed line in Figure 3*f*, consistent with the data for the other ray bundles.

INVERSION OF THE MONO CRATERS DATA: METHOD

To investigate the low-velocity anomaly in more detail, we inverted the relative residuals using a modified version of the "ACH" inversion technique first described by *Aki et al.* [1977]. In this section we briefly outline the method, which is described in great detail by *Ellsworth* [1977], *Aki et al.* [1977] *Iyer et al.* [1981*a*, *b*], and many other authors. Results of this modeling are given in the following section.

In this method the volume of interest below the seismic array is parameterized by dividing it into plane layers and dividing each layer into a grid of rectangular blocks. An initial average compressional wave velocity is assigned to each layer for purposes of ray tracing, but the results are not very sensitive to these initial velocities [*Aki et al.*, 1977]. The block sizes are governed by the station spacing of the network and the wavelength of the recorded compressional waves (both about 6 km).

This version of the ACH method uses plane waves incident on the bottom of the layered model. To linearize the equations, each segment of ray is assigned to the block in which it travels and refraction by the anomalous structure is disregarded. The linear equations can be expressed in matrix form as

$$Am = d \tag{5}$$

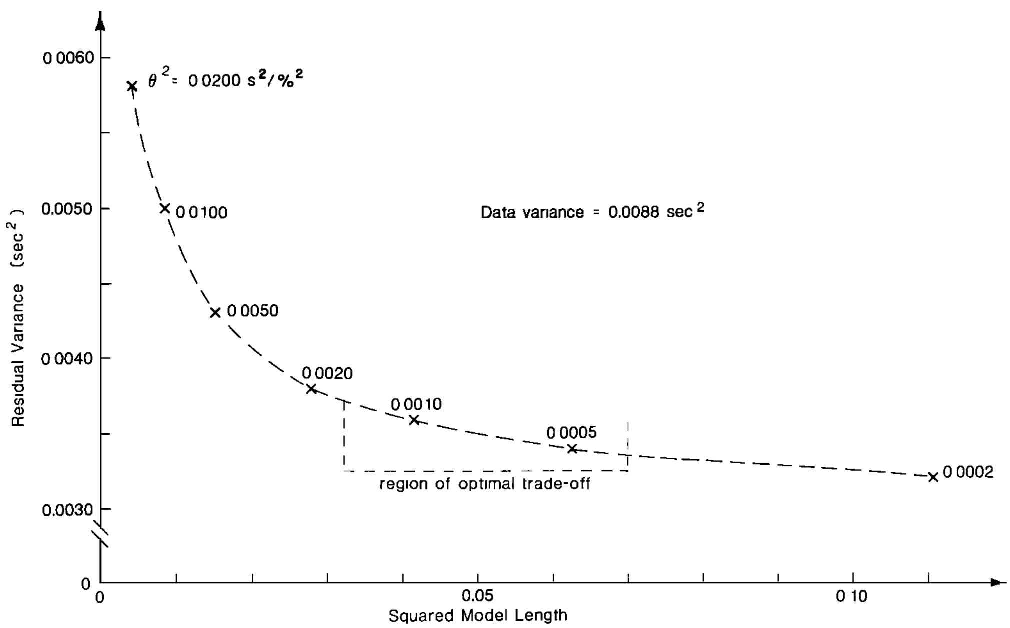

Fig. 4. Residual variance (i.e., model misfit) versus the length (i.e., complexity) of the solution vector ($\|\hat{m}\|$) showing the trade-off between these factors for a range of damping parameters θ^2.

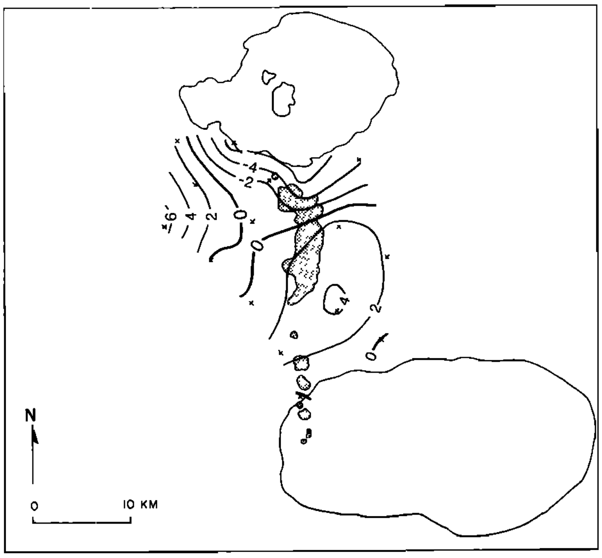

MODEL A LAYER 1 0.0 - 2.0 KM VELOCITY 4.50 KM/S

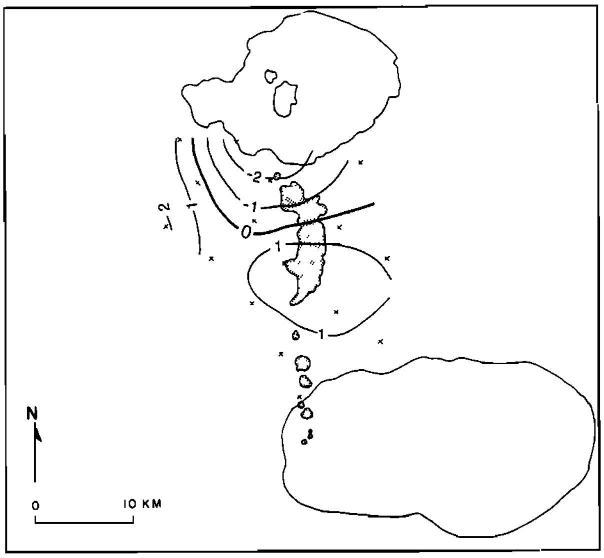

MODEL B LAYER 1 0 0 - 2.0 KM VELOCITY 3 38 - 5.40 KM/S

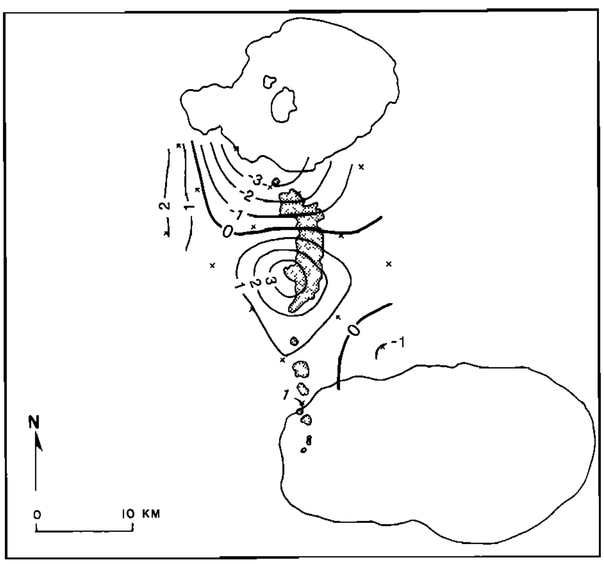

MODEL C LAYER 1 0.0 - 2.0 KM VELOCITY 3.38 - 5.40 KM/S

Fig. 5*a*

where m is a vector containing the unknown fractional slowness perturbations, $\mathbf{A}$ is a semidefinite matrix with the calculated unperturbed travel times of ray segments, and d is a vector containing the travel time residuals. $\mathbf{A}^T\mathbf{A}$ is singular because, for example, a uniform velocity perturbation in one layer is indistinguishable from origin time changes [*Aki and Lee*, 1976]. Thus to solve these equations we use the method of damped least squares [*Levenberg*, 1944; *Franklin*, 1970]:

$$\hat{m} = (\mathbf{A}^T\mathbf{A} + \theta^2\mathbf{I})^{-1}\mathbf{A}^T d \tag{6}$$

where $\hat{m}$ is the model estimate, $\theta^2 \approx \sigma d^2/\sigma m^2$ is the damping parameter [*Aki et al.*, 1977], and σd^2 and σm^2 are the estimated variances of the data and the true model m. The solution of the linearized problem gives the velocity perturbation of each block (approximated as the negative of the slowness perturbation) relative to an unknown mean layer velocity. Absolute velocities are indeterminate because relative, rather than absolute, residuals must be used and by reason of the singularity argument given above.

To examine the problems of velocity anomalies arising from near-surface sediments and of the trade-off between resolution and block size, we present three slightly different models. All three models have five layers; in the first layer the block structure is replaced by a separate first-layer "block" for each station. The reason for this special treatment is that in the first layer the rays arriving at a given station generally sample a volume through which rays to no other station pass.

Tables 2*a* and 2*b* show layer thicknesses, initial velocities, and block sizes for each model. The initial velocities and the thickness of the first layer were obtained from refraction profiles in the Mono basin area [*Pakiser*, 1976], and the Long Valley caldera area [*Hill*, 1976; *Kissling et al.*, 1984]. Model A has a uniform initial velocity assigned to all stations in layer 1, that is, no sediment corrections. The calculated velocity perturbations in layer 1 of model A were used to estimate the first-layer velocity corrections subsequently used in models B and C (Table 2*b*). These corrections produce travel time variations that are in the same sense but smaller than *Pakiser*'s [1976] refraction time terms for Mono basin (presumably because teleseismic rays have steeper angles of incidence, i.e., are shorter than refraction rays). The sediment corrections reduce the starting data variance, of course, but they also improve the fit of the calculated model to the data. That is, they reduce the unmodeled-data variance, the part of the data left unexplained by the model ("remaining varience" in Table 2*a*; see the appendix).

For layers 2–5 the blocks have horizontal dimensions of 5 km in models A and B and 6 km in model C. These dimensions are appropriate for the station spacing and give the good resolution characteristics discussed later. The height of the blocks was chosen to be 1.5 times the horizontal block size in a compromise between steep ray angles and block equidimensionality [cf. *Ellsworth and Koyanagi*, 1977]. To improve the resolution, only blocks sampled by at least 10 rays were used in the inversion.

Different damping factors (between $\theta^2 = 0.0200$ and 0.0002

Fig. 5. (opposite) Velocity models produced by ACH inversion method. The same layer of three models (A, B, and C) are shown in each figure; the depth range of model C is slightly different from the others (Table 2*a*). Contour intervals vary from model to model and layer to layer. They are labeled in percent (negative indicates slow). (*a*) Layer one (small crosses show station locations); (*b*)–(*e*) layers 2–5 (small crosses show block centers). Cross section in Plate 1 taken along line shown in Figure 5*c* for model B.

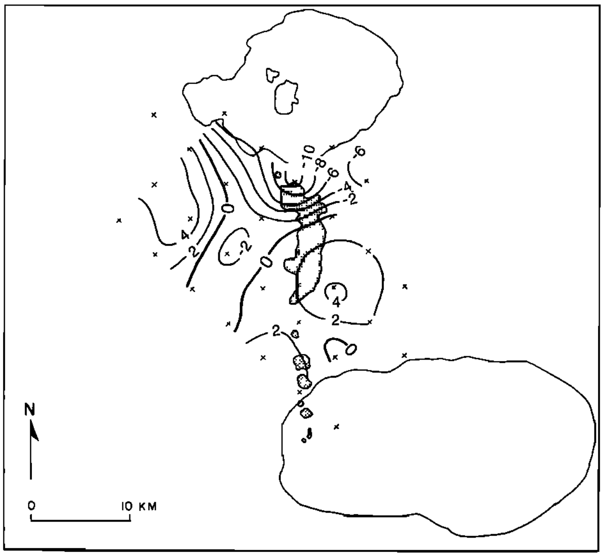

MODEL A LAYER 2 2.0 - 9.5 KM VELOCITY 6.00 KM/S

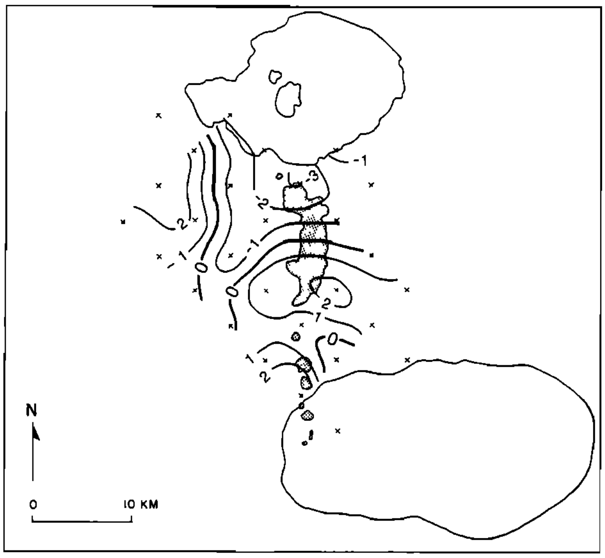

MODEL B LAYER 2 2.0 - 9.5 KM VELOCITY 6.00 KM/S

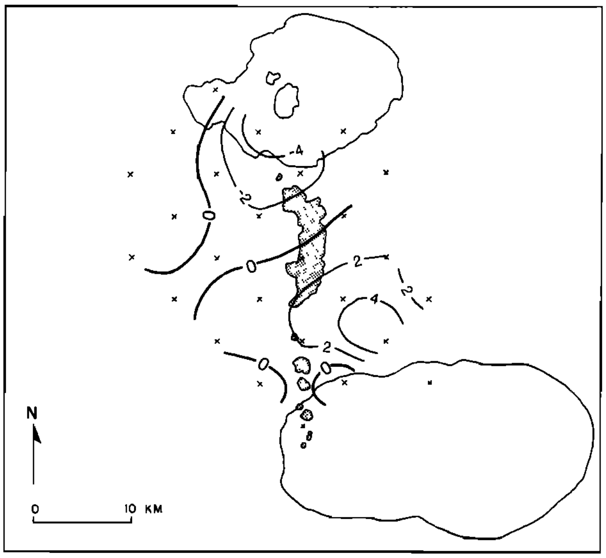

MODEL C LAYER 2 2.0 - 11.0 KM VELOCITY 6.00 KM/S

Fig. 5*b*

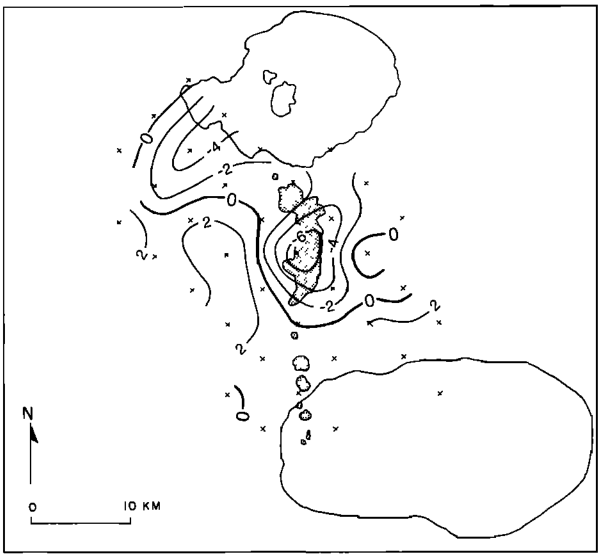

MODEL A LAYER 3 9.5 - 17.0 KM VELOCITY 6.25 KM/S

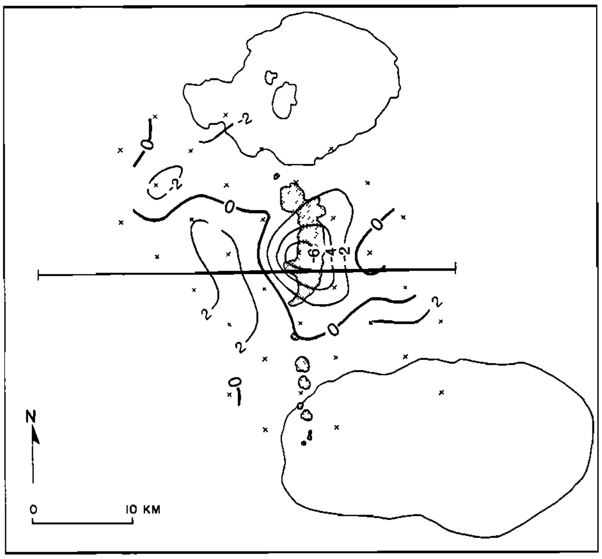

MODEL B LAYER 3 9.5 - 17.0 KM VELOCITY 6.25 KM/S

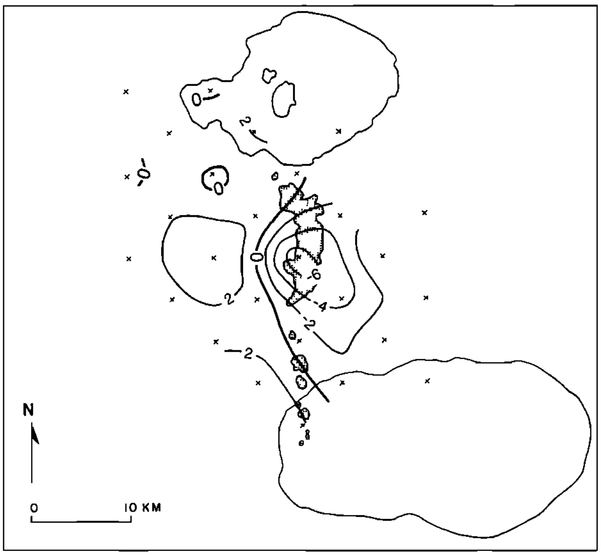

MODEL C LAYER 3 11.0 - 20.0 KM VELOCITY 6.25 KM/S

Fig. 5*c*

Fig. 5. (continued)

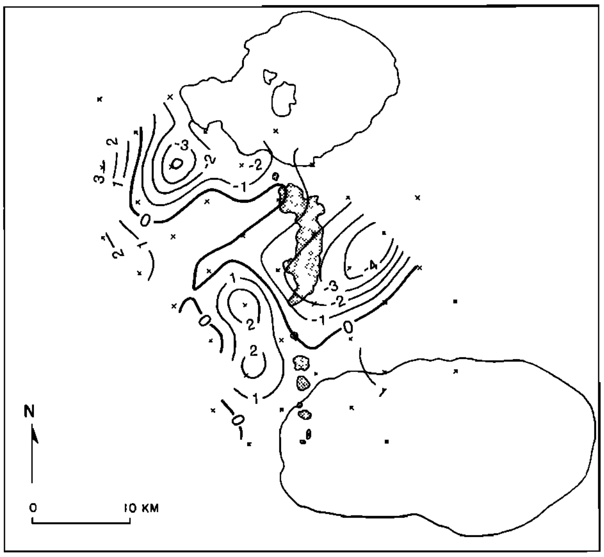

MODEL A LAYER 4 17.0 - 24.5 KM VELOCITY 6.50 KM/S

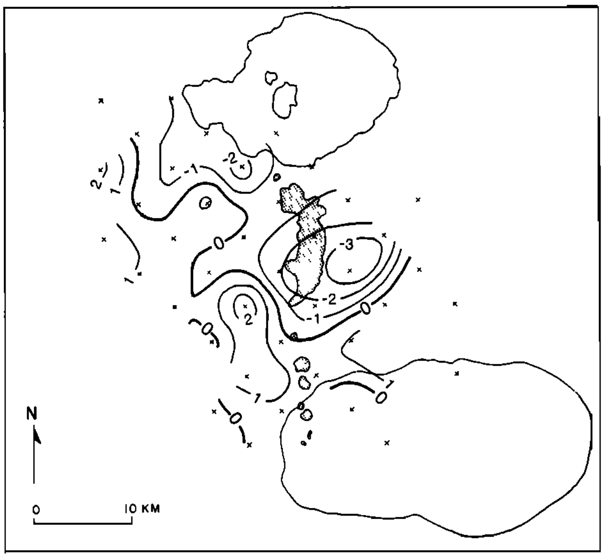

MODEL B LAYER 4 17.0 - 24.5 KM VELOCITY 6.50 KM/S

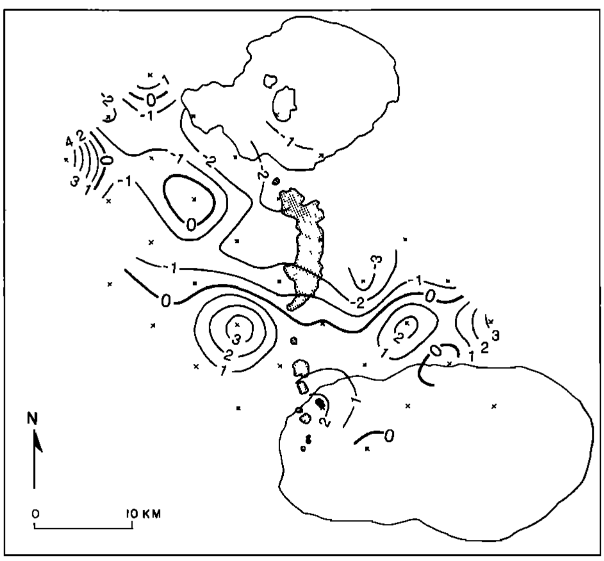

MODEL C LAYER 4 20.0 - 29.0 KM VELOCITY 6 50 KM/S

Fig. 5*d*

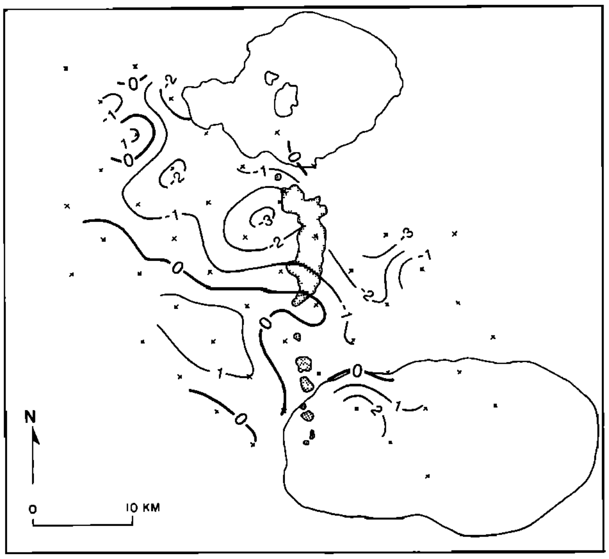

MODEL A LAYER 5 24.5 -32.0 KM VELOCITY 6.90 KM/S

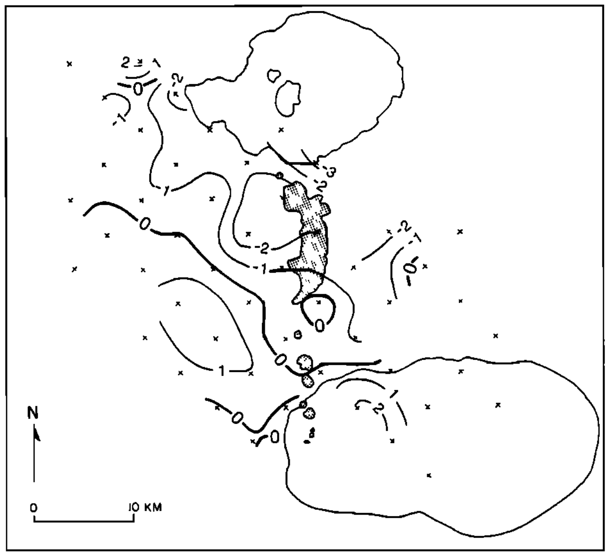

MODEL B LAYER 5 24.5 - 32.0 KM VELOCITY 6.90 KM/S

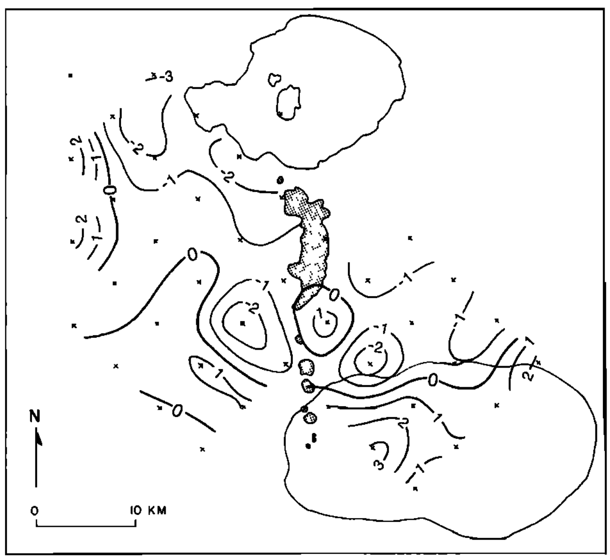

MODEL C LAYER 5 29.0 - 38.0 KM VELOCITY 6.90 KM/S

Fig. 5*e*

Fig. 5. (continued)

Legend:

Station name	Block number
Velocity perturbation	
Number of hits (rays)	
Diagonal of the resolution matrix	
Standard errors	

Layer 1:

mc1 1 6.38 69 0.3211 0.66	mc2 2 -0.11 70 0.2505 0.60	mc3 3 0.48 81 0.2874 0.64	mc4 4 2.31 71 0.2727 0.58
m5a 5 -0.29 21 0.2171 0.79	m5b 6 0.08 40 0.2523 0.73	mc6 7 1.49 63 0.3344 0.69	mc7 8 2.53 56 0.2947 0.74
m8a 9 -0.19 19 0.1405 0.68	m8b 10 -0.24 53 0.2377 0.73	mc9 11 1.58 37 0.2237 0.67	mca 12 4.07 68 0.3116 0.70
mcb 13 -0.31 67 0.2599 0.62	mcc 14 -6.53 43 0.1380 0.48	md1 15 -1.94 15 0.0946 0.58	md2 16 -5.78 41 0.1554 0.58
mce 17 3.31 79 0.2393 0.59	mcf 18 1.57 80 0.2990 0.63	mcg 19 -4.19 42 0.1316 0.41	20

Layer 2:

21 0	22 4	23 3.26 26 0.4709 0.74	24 0	25 0
26 2.17 22 0.1775 0.65	27 4.92 33 0.4826 0.92	28 2.82 77 0.6783 0.69	29 -7.94 25 0.5185 0.78	30 0
31 3.31 23 0.4335 0.71	32 4.74 74 0.6471 0.77	33 -0.37 50 0.5698 0.85	34 -6.74 24 0.3675 0.90	35 0
36 -0.27 18 0.2991 0.72	37 -2.38 99 0.5888 0.75	38 -1.86 69 0.6577 0.78	39 -10.38 46 0.6127 0.80	40 -4.83 18 0.4664 0.86
41 -0.49 35 0.4370 0.74	42 0.76 95 0.6369 0.73	43 1.39 63 0.4784 0.86	44 0.34 79 0.6617 0.70	45 -6.72 29 0.5508 0.84
46 3.64 69 0.6126 0.60	47 1.30 42 0.3515 0.74	48 4.22 53 0.6261 0.79	49 2.18 72 0.7005 0.65	50 5
51 2.77 58 0.6310 0.68	52 -0.39 15 0.1607 0.64	53 2.05 55 0.6970 0.69	54 1.81 21 0.5139 0.75	55 2
56 -2.33 10 0.2652 0.76	57 2	58 2.01 17 0.5035 0.71	59 2	60 0

Layer 3:

61 0	62 0	63 0	64 9	65 0	66 0	67 0
68 0	69 5	70 1.44 20 0.4531 0.93	71 0.60 28 0.3739 0.79	72 9	73 0	74 0
75 0	76 3.97 28 0.5296 0.76	77 -2.17 42 0.6125 0.78	78 -4.65 43 0.4936 0.82	79 -4.69 20 0.4062 0.86	80 0	81 0
82 4	83 1.34 29 0.4537 0.83	84 1.53 45 0.5651 0.88	85 -0.75 53 0.6296 0.79	86 -2.68 20 0.4717 0.88	87 3	88 2
89 0	90 1.17 39 0.5101 0.81	91 3.44 67 0.6923 0.77	92 0.00 39 0.5876 0.86	93 -1.08 40 0.5930 0.88	94 -4.09 20 0.4029 0.79	95 2
96 0	97 3.40 51 0.5909 0.74	98 1.07 44 0.6026 0.81	99 -6.87 61 0.6940 0.77	100 -5.11 52 0.6254 0.82	101 -1.29 12 0.1793 0.75	102 2
103 -0.14 15 0.1674 0.65	104 0.82 54 0.5535 0.79	105 -0.06 50 0.5740 0.75	106 -3.90 69 0.6602 0.82	107 0.80 65 0.5200 0.83	108 -0.69 11 0.4417 0.94	109 2
110 0.77 16 0.3675 0.69	111 1.52 32 0.4461 0.81	112 1.41 31 0.5428 0.80	113 1.99 44 0.5029 0.86	114 -0.44 27 0.4136 0.86	115 5	116 0
117 1	118 0.49 11 0.3327 0.73	119 8	120 2.46 25 0.3659 0.84	121 3.24 14 0.3738 0.94	122 2	123 0
124 0	125 3	126 1	127 0.61 13 0.3127 0.82	128 1	129 0	130 0

Layer 4:

131 0	132 0	133 5	134 1.36 18 0.2907 0.72	135 8	136 1	137 0	138 0
139 0	140 1	141 3.01 35 0.4984 0.86	142 0.17 33 0.4707 0.87	143 -2.43 17 0.3683 0.78	144 2	145 0	146 0
147 1	148 2.20 14 0.3597 0.80	149 -0.50 47 0.5722 0.83	150 -3.90 33 0.5043 0.81	151 -1.55 16 0.4260 0.90	152 6	153 2	154 0
155 3	156 1.31 21 0.4433 0.83	157 0.55 43 0.5320 0.86	158 0.78 38 0.5525 0.85	159 -2.04 37 0.5801 0.83	160 -0.49 13 0.3692 0.89	161 2	162 0
163 1	164 0.08 25 0.4849 0.82	165 -0.13 52 0.6564 0.81	166 -0.10 39 0.5540 0.88	167 0.12 50 0.5651 0.86	168 -1.61 26 0.4458 0.87	169 2	170 0
171 4	172 -0.60 33 0.5502 0.87	173 2.75 48 0.6639 0.82	174 -1.80 68 0.6380 0.84	175 -2.05 44 0.5719 0.87	176 -1.76 21 0.4119 0.98	177 0	178 1
179 -0.74 15 0.1379 0.61	180 2.00 33 0.4830 0.87	181 0.70 45 0.5605 0.83	182 -2.14 65 0.6432 0.83	183 -4.18 50 0.5918 0.84	184 -4.38 15 0.3772 0.85	185 0.68 11 0.3592 0.88	186 1
187 0.06 11 0.2930 0.65	188 0.52 12 0.2446 0.79	189 0.00 43 0.5052 0.82	190 0.72 32 0.5040 0.89	191 0.02 13 0.3699 0.95	192 0.16 17 0.4140 0.82	193 8	194 0
195 1	196 0	197 0.00 21 0.3884 0.83	198 1.37 20 0.4290 0.83	199 7	200 0.56 23 0.3949 0.83	201 1	202 0
203 0	204 1	205 -0.61 13 0.2467 0.66	206 6	207 0.43 12 0.2871 0.75	208 5	209 0	210 0

Layer 5:

211 0	212 0	213 3	214 3.53 13 0.2756 0.81	215 7	216 1	217 0	218 0
219 0	220 0	221 8	222 -0.93 18 0.3912 0.88	223 1.19 12 0.2939 0.82	224 2	225 0	226 0
227 0	228 -0.62 10 0.2111 0.82	229 -0.53 41 0.6204 0.86	230 1.02 23 0.4505 0.89	231 -2.53 17 0.4049 0.87	232 5	233 1	234 1
235 0.71 15 0.2981 0.85	236 0.59 23 0.4454 0.93	237 -1.20 44 0.5880 0.89	238 -2.01 34 0.5352 0.88	239 -1.52 23 0.4162 0.90	240 5	241 2	242 1
243 8	244 0.09 18 0.4082 0.95	245 -0.37 40 0.6097 0.90	246 -1.19 32 0.5166 0.94	247 -0.88 38 0.4305 0.93	248 -0.29 13 0.3793 0.90	249 3	250 1
251 0.00 15 0.3879 0.95	252 1.41 51 0.6074 0.92	253 -0.63 40 0.5161 0.96	254 -2.52 43 0.5733 0.93	255 -2.80 45 0.6060 0.89	256 0.81 13 0.3514 0.89	257 3	258 0
259 0.15 18 0.4555 0.94	260 1.82 41 0.5056 0.93	261 0.79 37 0.5302 0.99	262 -0.53 73 0.6197 0.88	263 -1.76 30 0.5318 0.91	264 8	265 3	266 0
267 -0.35 17 0.5167 0.88	268 0.97 31 0.3796 0.94	269 -0.85 46 0.5793 0.92	270 0.23 58 0.6762 0.85	271 -2.23 23 0.5067 0.98	272 -3.96 10 0.3147 0.85	273 6	274 2
275 -0.04 10 0.2403 0.67	276 -0.01 10 0.2490 0.79	277 -0.41 34 0.5280 0.88	278 -1.10 18 0.4957 0.93	279 -1.90 17 0.4745 0.94	280 -0.03 14 0.3183 0.86	281 -1.37 11 0.1970 0.71	282 4
283 1	284 3	285 2.49 15 0.3326 0.84	286 -0.20 21 0.4541 0.91	287 6	288 -1.19 23 0.3361 0.79	289 5	290 2
291 0	292 1	293 1.41 17 0.3230 0.80	294 1.28 17 0.3121 0.89	295 1.45 10 0.3166 0.90	296 0.80 20 0.2245 0.78	297 3	298 0
299 0	300 1	301 -1.38 11 0.1723 0.71	302 5	303 0.90 14 0.2566 0.70	304 5	305 0	306 0

Fig. 6*a*. Model A. Note that layers 2–5 are shown in approximately correct geographic arrangement, though the blocks should be square. The plus corresponds to the "model center" in Figure 1; the top of the figure is "northwest." For layer 1, compare station names with Figure 1.

Legend:

Station name Block number Velocity perturbation Number of hits (rays) Diagonal of the resolution matrix Row 99 of the resolution matrix Standard errors Row 99 of the covarience matrix

Layer 1:

mc1 1 2.01 69 0.2564 -0.0019 0.54 0.071	mc2 2 0.75 70 0.2504 0.0060 0.53 0.085	mc3 3 0.91 81 0.2882 0.0126 0.57 0.200	mc4 4 0.12 71 0.2427 -0.0016 0.49 -0.001
m5a 5 0.25 21 0.2175 0.0001 0.70 -0.017	m5b 6 0.38 40 0.2533 -0.0005 0.65 -0.002	mc6 7 0.92 63 0.3203 -0.0014 0.61 -0.001	mc7 8 0.52 56 0.2605 -0.0029 0.63 0.085
m8a 9 -0.10 19 0.1406 0.0003 0.60 -0.034	m8b 10 -0.41 53 0.2372 0.0491 0.64 -0.273	mc9 11 1.78 37 0.2237 -0.0241 0.59 -0.218	mca 12 1.42 68 0.2765 0.0196 0.60 -0.082
mcb 13 0.52 67 0.2613 -0.0062 0.56 0.047	mcc 14 -2.45 43 0.2111 0.0078 0.50 0.122	md1 15 -1.92 15 0.1229 0.0015 0.57 0.031	md2 16 -1.57 41 0.2345 -0.0030 0.59 0.030
mce 17 0.53 79 0.2101 0.0371 0.50 -0.279	mcf 18 0.86 80 0.2881 0.0062 0.57 0.252	mcg 19 -0.76 42 0.1816 0.0005 0.41 0.023	20

Layer 2:

21 0	22 4	23 2.58 26 0.4791 0.0003 0.65 0.013	24 0	25 0
26 1.35 23 0.2076 0.0007 0.60 -0.002	27 2.90 34 0.5066 0.0003 0.82 -0.002	28 1.78 75 0.6850 0.0017 0.62 -0.004	29 -2.47 25 0.4839 -0.0005 0.67 -0.031	30 0
31 1.45 23 0.4372 0.0006 0.63 0.035	32 1.83 69 0.6531 -0.0023 0.69 0.140	33 -1.17 48 0.5646 -0.0104 0.76 0.359	34 -2.27 26 0.3565 0.0085 0.77 0.107	35 0
36 0.19 18 0.2976 -0.0008 0.64 0.033	37 -1.44 102 0.5868 0.0039 0.66 0.186	38 -1.59 72 0.6563 0.0713 0.69 -0.770	39 -3.03 46 0.5964 0.0104 0.68 0.317	40 -0.77 18 0.4034 -0.0008 0.74 -0.019
41 -0.17 36 0.4344 -0.0035 0.66 -0.062	42 1.61 95 0.6353 0.0082 0.64 0.089	43 1.03 64 0.4780 0.0978 0.76 -0.174	44 -1.13 75 0.6663 0.0603 0.63 -0.723	45 -1.64 33 0.5324 0.0020 0.71 0.085
46 1.37 69 0.6255 0.0004 0.54 0.011	47 0.54 42 0.3586 -0.0009 0.66 0.190	48 2.33 52 0.6364 0.0401 0.70 -0.274	49 0.18 72 0.7117 0.0009 0.58 0.376	50 5
51 2.97 58 0.6343 -0.0001 0.61 0.006	52 -0.79 15 0.1642 -0.0009 0.58 -0.016	53 1.49 56 0.6974 -0.0093 0.61 0.239	54 1.27 21 0.5173 -0.0013 0.67 -0.026	55 2
56 -2.02 10 0.2658 0.0000 0.67 -0.001	57 2	58 2.53 17 0.5037 0.0001 0.63 -0.003	59 2	60 0

Layer 3:

61 0	62 0	63 0	64 9	65 0	66 0	67 0
68 0	69 5	70 1.50 20 0.4605 -0.0014 0.82 -0.004	71 -0.14 27 0.3846 0.0003 0.72 0.003	72 9	73 0	74 0
75 3	76 1.57 28 0.5327 0.0010 0.68 -0.024	77 -2.38 42 0.6116 0.0012 0.69 -0.002	78 -1.74 41 0.4848 0.0033 0.73 -0.041	79 -2.47 20 0.3962 -0.0001 0.75 -0.020	80 0	81 0
82 5	83 0.38 29 0.4541 -0.0013 0.74 -0.093	84 1.91 42 0.5646 -0.0073 0.78 -0.195	85 -0.90 53 0.6294 -0.0248 0.70 -0.058	86 -0.44 20 0.4622 0.0011 0.79 -0.272	87 3	88 2
89 0	90 0.98 39 0.5104 -0.0024 0.72 -0.226	91 2.59 67 0.6910 -0.0387 0.68 -0.114	92 0.26 39 0.5918 -0.0516 0.77 -0.250	93 -0.93 41 0.5869 -0.0537 0.78 -0.147	94 -1.91 20 0.3963 -0.0030 0.68 -0.185	95 2
96 0	97 2.92 51 0.5917 -0.0029 0.65 -0.144	98 1.08 48 0.5947 -0.0250 0.72 -0.354	99 -6.93 61 0.6957 0.6957 0.68 4.727	100 -3.31 53 0.6285 -0.0518 0.73 -0.528	101 -1.00 13 0.1768 0.0009 0.66 -0.046	102 2
103 -0.12 15 0.1679 0.0004 0.58 0.035	104 0.83 53 0.5549 -0.0040 0.70 -0.177	105 -0.22 51 0.5721 -0.0309 0.66 -0.302	106 -3.58 68 0.6604 -0.0771 0.73 -0.214	107 1.00 65 0.5204 -0.0395 0.74 -0.492	108 0.32 11 0.4384 -0.0059 0.84 -0.114	109 2
110 1.00 16 0.3680 -0.0004 0.62 -0.003	111 1.31 33 0.4502 -0.0017 0.72 -0.085	112 1.19 31 0.5437 -0.0037 0.72 -0.199	113 1.91 44 0.4994 -0.0074 0.77 -0.211	114 -0.82 27 0.4127 -0.0018 0.76 -0.104	115 5	116 0
117 1	118 0.85 11 0.3343 0.0001 0.65 0.001	119 8	120 2.29 25 0.3644 0.0009 0.75 -0.019	121 3.22 14 0.3722 0.0000 0.83 -0.004	122 2	123 0
124 0	125 3	126 1	127 0.57 13 0.3128 0.0009 0.72 0.024	128 1	129 0	130 0

Layer 4:

131 0	132 0	133 5	134 0.93 18 0.2929 0.0000 0.64 -0.004	135 8	136 1	137 0	138 0
139 0	140 2	141 2.02 35 0.4933 -0.0009 0.76 -0.012	142 -0.48 33 0.4712 0.0009 0.77 0.000	143 -1.10 17 0.3627 -0.0006 0.69 0.005	144 1	145 0	146 0
147 4	148 1.88 15 0.3557 -0.0005 0.71 -0.002	149 -0.16 47 0.5692 0.0001 0.74 -0.041	150 -1.20 32 0.4982 -0.0069 0.72 -0.090	151 -1.36 16 0.4179 -0.0023 0.80 -0.077	152 6	153 2	154 0
155 4	156 0.90 20 0.4309 0.0002 0.74 0.035	157 0.44 43 0.5314 0.0027 0.76 0.078	158 1.13 38 0.5492 -0.0248 0.75 0.175	159 -2.30 38 0.5747 -0.0037 0.74 0.097	160 -0.41 13 0.3637 -0.0035 0.79 0.086	161 2	162 0
163 1	164 0.16 25 0.4852 -0.0002 0.73 0.065	165 -0.32 53 0.6556 0.0030 0.72 0.193	166 -0.32 39 0.5547 0.0089 0.78 -0.060	167 -0.20 50 0.5741 0.0184 0.76 0.172	168 -0.83 26 0.4440 0.0042 0.77 0.079	169 2	170 0
171 4	172 -0.18 34 0.5517 0.0006 0.77 0.068	173 2.45 47 0.6558 0.0012 0.73 0.205	174 -1.90 68 0.6402 0.1294 0.74 -1.600	175 -2.20 44 0.5702 0.0466 0.77 0.071	176 -1.02 20 0.4132 0.0037 0.87 0.321	177 0	178 1
179 -0.59 15 0.1497 0.0001 0.56 0.019	180 1.70 33 0.4827 0.0013 0.77 0.048	181 0.31 45 0.5618 0.0043 0.74 0.148	182 -1.83 65 0.6449 0.0198 0.73 0.144	183 -3.53 50 0.5916 0.0531 0.75 -0.417	184 -2.47 15 0.3769 0.0078 0.76 0.213	185 1.46 11 0.3568 -0.0066 0.77 -0.071	186 1
187 0.00 11 0.2931 -0.0003 0.58 0.010	188 0.73 12 0.2447 0.0004 0.70 0.018	189 0.71 43 0.5045 0.0065 0.73 0.060	190 1.11 32 0.4996 0.0046 0.78 0.027	191 0.51 12 0.3623 -0.0090 0.84 0.134	192 0.49 16 0.4185 0.0034 0.74 0.154	193 8	194 0
195 1	196 0	197 -0.91 21 0.3893 0.0006 0.74 0.062	198 1.18 20 0.4308 -0.0008 0.74 -0.033	199 7	200 0.28 23 0.4037 -0.0008 0.74 -0.024	201 2	202 0
203 0	204 1	205 -0.73 13 0.2514 0.0005 0.59 0.023	206 6	207 0.13 12 0.2872 0.0003 0.67 -0.008	208 5	209 0	210 0

Layer 5:

211 0	212 0	213 4	214 2.97 13 0.2752 -0.0003 0.72 -0.010	215 7	216 1	217 0	218 0
219 0	220 0	221 8	222 -1.15 19 0.3843 0.0000 0.78 -0.016	223 2.15 12 0.2972 -0.0014 0.73 -0.036	224 2	225 0	226 0
227 0	228 -0.48 10 0.2115 -0.0002 0.73 0.001	229 -0.20 40 0.6177 0.0003 0.76 0.010	230 -0.31 23 0.4424 -0.0043 0.79 0.020	231 -2.21 17 0.4019 -0.0019 0.78 -0.024	232 5	233 1	234 1
235 -0.03 15 0.3092 0.0000 0.75 0.008	236 0.84 23 0.4566 -0.0001 0.82 -0.031	237 -0.53 40 0.5879 0.0038 0.79 -0.044	238 -1.43 34 0.5383 -0.0109 0.78 0.233	239 -1.22 23 0.4210 -0.0044 0.80 0.070	240 6	241 2	242 1
243 8	244 0.40 18 0.4047 -0.0023 0.84 -0.033	245 0.02 40 0.6128 0.0000 0.80 0.044	246 -0.14 32 0.5200 0.0202 0.83 0.125	247 -1.68 37 0.4322 0.0040 0.82 0.086	248 -0.36 13 0.3793 0.0043 0.79 0.123	249 3	250 1
251 0.24 15 0.3878 -0.0003 0.84 0.031	252 1.73 51 0.6098 -0.0020 0.82 0.038	253 0.17 38 0.5176 0.0031 0.85 -0.128	254 -2.65 43 0.5786 0.0672 0.82 -0.615	255 -3.02 45 0.6027 0.0153 0.79 0.086	256 0.06 13 0.3613 0.0051 0.79 0.115	257 3	258 0
259 0.50 19 0.4562 -0.0009 0.84 0.018	260 1.82 42 0.5069 0.0032 0.82 0.140	261 0.43 36 0.5357 0.0184 0.87 -0.008	262 -0.96 73 0.6206 0.0148 0.78 -0.239	263 -1.97 30 0.5309 -0.0088 0.81 0.054	264 8	265 3	266 0
267 -0.16 17 0.5174 0.0002 0.78 0.036	268 0.87 30 0.3771 0.0055 0.84 0.162	269 -0.52 46 0.5788 0.0061 0.81 0.110	270 0.29 58 0.6832 0.0263 0.74 -0.186	271 -1.90 23 0.5102 0.0275 0.87 -0.203	272 -2.18 10 0.3155 0.0096 0.75 0.233	273 6	274 2
275 -0.03 10 0.2404 -0.0001 0.60 0.009	276 -0.07 10 0.2490 0.0000 0.70 0.018	277 0.20 34 0.5277 0.0064 0.78 0.059	278 -1.17 18 0.4951 0.0087 0.82 -0.074	279 -1.18 17 0.4724 0.0461 0.83 -0.467	280 0.45 13 0.3011 0.0037 0.76 0.277	281 -0.53 11 0.1911 0.0012 0.62 0.083	282 4
283 1	284 3	285 1.95 15 0.3237 0.0014 0.74 0.036	286 0.36 21 0.4512 0.0063 0.81 0.063	287 6	288 -0.82 23 0.3335 0.0006 0.70 0.021	289 5	290 2
291 0	292 1	293 1.50 17 0.3233 -0.0024 0.71 -0.016	294 0.83 18 0.3228 0.0011 0.79 0.040	295 0.91 10 0.3177 0.0004 0.80 -0.037	296 1.02 20 0.2161 -0.0009 0.68 -0.037	297 3	298 0
299 0	300 1	301 -1.38 11 0.1772 0.0003 0.64 0.005	302 5	303 0.74 14 0.2567 0.0001 0.62 -0.011	304 5	305 0	306 0

Fig. 6*b*. Model B. See Figure 6*a* caption.

Legend:

Station name	Block number
Velocity perturbation	
Number of hits (rays)	
Diagonal of the resolution matrix	
Standard errors	

Layer 1:

mc1 1 1.83 69 0.2985 0.86	mc2 2 0.34 70 0.2710 0.86	mc3 3 0.87 81 0.3226 0.91	mc4 4 0.97 71 0.4308 1.00	m5a 5 1.13 21 0.3271 1.05
m5b 6 0.73 40 0.3468 0.99	mc6 7 1.64 63 0.3188 0.84	mc7 8 0.53 56 0.3487 0.98	m8a 9 -0.10 19 0.2292 0.98	m8b 10 -0.31 53 0.3424 1.05
mc9 11 3.67 37 0.3077 0.98	mca 12 0.56 68 0.3027 0.87	mcb 13 -1.25 67 0.2366 0.74	mcc 14 -3.93 43 0.2981 0.86	md1 15 -2.81 15 0.2144 0.99
md2 16 -2.28 41 0.3226 0.97	mce 17 0.41 79 0.2612 0.81	mcf 18 0.40 80 0.2855 0.80	mcg 19 -0.70 42 0.2025 0.58	20

Layer 2:

21 0	22 0	23 8	24 0	25 0
26 0	27 1.68 23 0.1875 0.71	28 1.28 69 0.7189 0.77	29 1.00 14 0.2938 0.97	30 0
31 0.37 19 0.2692 0.79	32 1.95 90 0.7664 0.76	33 -0.99 87 0.7812 0.78	34 -4.98 40 0.6265 0.98	35 0
36 -0.23 13 0.1054 0.70	37 -0.48 109 0.7780 0.70	38 -1.79 83 0.8208 0.71	39 -2.87 50 0.7300 0.83	40 -0.61 17 0.6300 1.01
41 0.18 32 0.2606 0.96	42 1.24 116 0.7879 0.70	43 0.55 81 0.7174 0.88	44 -0.14 92 0.7777 0.74	45 -1.28 32 0.6736 0.85
46 -0.89 44 0.7446 0.88	47 1.96 85 0.7439 0.82	48 3.59 94 0.7490 0.78	49 2.20 90 0.7905 0.67	50 3
51 1.03 42 0.7608 0.80	52 -1.46 23 0.2273 0.84	53 5.49 72 0.7651 0.73	54 1.20 19 0.3991 1.00	55 0
56 3	57 0	58 -1.45 13 0.2700 0.93	59 0	60 0

Layer 3:

61 0	62 0	63 0	64 2	65 0	66 0	67 0
68 0	69 0	70 7	71 2.99 26 0.7279 1.00	72 3	73 0	74 0
75 0	76 4	77 -0.37 57 0.7000 0.87	78 1.19 49 0.7000 0.95	79 -0.40 15 0.5361 1.09	80 0	81 0
82 0	83 1.45 25 0.5943 0.81	84 1.82 56 0.7476 0.89	85 -0.11 62 0.7785 0.83	86 2.11 21 0.6607 1.07	87 4	88 0
89 0	90 1.66 34 0.6804 0.98	91 3.73 67 0.8257 0.74	92 1.44 61 0.8096 0.80	93 0.43 52 0.8094 0.83	94 -1.57 15 0.5516 1.10	95 0
96 0	97 1.91 55 0.7735 0.78	98 0.99 59 0.8084 0.79	99 -6.53 78 0.8260 0.73	100 -2.60 48 0.8145 0.81	101 8	102 1
103 6	104 3.38 46 0.7034 0.93	105 -0.74 62 0.8034 0.79	106 -4.47 75 0.8194 0.75	107 0.16 45 0.7182 0.95	108 2.03 13 0.5995 1.13	109 0
110 6	111 2.32 18 0.4879 1.17	112 -1.48 42 0.7577 0.85	113 -0.81 31 0.6998 0.93	114 -1.33 28 0.5433 0.92	115 3	116 0
117 0	118 9	119 9	120 0.87 15 0.5646 0.92	121 7	122 0	123 0
124 0	125 1	126 0	127 6	128 0	129 0	130 0

Layer 4:

131 0	132 0	133 1	134 9	135 3	136 1	137 0	138 0
139 0	140 0	141 4.80 17 0.5485 1.03	142 -2.15 25 0.6337 1.00	143 2.02 14 0.6140 1.06	144 1	145 0	146 0
147 0	148 8	149 -1.47 53 0.7234 0.91	150 -0.85 44 0.7002 0.94	151 -2.32 21 0.5847 1.03	152 4	153 2	154 0
155 0	156 0.98 22 0.6274 1.01	157 -1.80 56 0.7378 0.92	158 0.98 42 0.7445 0.90	159 -2.86 37 0.6737 0.94	160 -0.52 13 0.6027 1.14	161 2	162 0
163 0	164 0.33 27 0.6424 0.97	165 -0.49 76 0.7840 0.86	166 -2.35 58 0.7766 0.89	167 -1.97 61 0.7877 0.83	168 -0.99 19 0.6424 1.12	169 2	170 0
171 0	172 0.18 26 0.6591 0.93	173 3.39 64 0.7900 0.84	174 -1.49 95 0.8307 0.77	175 -2.63 52 0.7953 0.85	176 6	177 2	178 1
179 8	180 0.07 28 0.6456 0.98	181 0.21 55 0.7797 0.87	182 -0.15 80 0.7870 0.84	183 -3.12 47 0.7351 0.93	184 -1.76 11 0.6030 1.02	185 7	186 1
187 5	188 8	189 2.21 23 0.6406 1.02	190 0.28 38 0.6923 0.95	191 2.06 23 0.5767 0.96	192 -1.58 17 0.4960 0.97	193 7	194 0
195 0	196 0	197 -0.27 19 0.6147 0.97	198 0.66 20 0.5855 1.05	199 -0.49 13 0.4753 1.00	200 3.20 21 0.4669 0.97	201 0	202 0
203 0	204 1	205 5	206 5	207 2.08 11 0.5684 1.13	208 4	209 0	210 0

Layer 5:

211 0	212 0	213 1	214 6	215 3	216 1	217 0	218 0
219 0	220 0	221 6	222 1.66 18 0.5332 1.06	223 8	224 1	225 0	226 0
227 0	228 5	229 2.99 34 0.7243 0.98	230 -1.46 27 0.6594 1.03	231 -3.05 19 0.5842 1.13	232 4	233 2	234 0
235 3	236 2.46 17 0.6135 1.10	237 0.04 56 0.7543 0.90	238 -2.01 34 0.7205 0.97	239 -0.99 28 0.5903 1.05	240 6	241 2	242 0
243 0.00 12 0.2893 1.05	244 -0.93 28 0.6368 1.05	245 -0.67 63 0.8043 0.86	246 -0.16 38 0.7383 0.98	247 -2.43 34 0.7120 0.98	248 -1.13 12 0.5890 1.12	249 1	250 0
251 0.29 10 0.3163 1.06	252 0.43 37 0.7323 0.96	253 0.50 54 0.8063 0.86	254 -0.93 54 0.7839 0.90	255 -1.90 44 0.7807 0.90	256 6	257 2	258 0
259 -0.14 15 0.4900 1.16	260 1.04 34 0.7403 0.95	261 -2.59 57 0.7857 0.91	262 -0.68 66 0.8207 0.82	263 -0.54 29 0.6532 1.11	264 9	265 2	266 0
267 -0.51 19 0.6654 1.03	268 0.90 28 0.6151 1.11	269 -1.22 39 0.7538 0.96	270 1.33 53 0.8225 0.81	271 -1.46 26 0.7392 0.99	272 -1.48 11 0.4468 1.17	273 3	274 2
275 4	276 3	277 0.80 19 0.6811 1.04	278 -2.45 31 0.7005 1.03	279 -0.16 26 0.7018 0.99	280 -0.63 12 0.4882 1.12	281 9	282 1
283 1	284 1	285 3.12 15 0.6013 1.10	286 1.50 25 0.6619 1.01	287 -0.85 16 0.4669 1.01	288 -1.55 21 0.4978 0.84	289 4	290 1
291 0	292 0	293 0.16 11 0.4173 1.07	294 0.97 14 0.5542 1.09	295 0.66 15 0.4856 0.98	296 2.35 14 0.4704 1.08	297 2	298 0
299 0	300 1	301 3	302 3	303 9	304 5	305 0	306 0

Fig. 6*c*. Model C. See Figure 6*a* caption.

$s^2/\%^2$) were tested to investigate the trade-offs between resolution, standard errors, the fit to the observations, and smoothing of the result. For the final models, $\theta^2 = 0.0010$ $s^2/\%^2$ (models A and B) and 0.0005 $s^2/\%^2$ (model C) were adopted. In our opinion these values give the optimal trade-off, though the value chosen for this ad hoc parameter is essentially arbitrary. For damping parameters smaller than $\theta^2 = 0.0005$ $s^2/\%^2$ the increase of the standard errors and of model length (i.e., model complexity) did not compare favorably with the small improvement grained in the fit (Figure 4). For damping factors larger than $\theta^2 = 0.0010$ $s^2/\%^2$ the decrease in the fit is large compared to a small improvement in smoothing.

With another series of models (not presented here) we investigated the influence of block size, layer thickness, and block position on the pattern of highs and lows seen in the calculated models. Even though the magnitudes of the perturbations change (because the block boundaries are nonphysical and artifically influence the result), all models tested showed the same major features. Therefore we believe that the ensemble of models presented here fairly represents the set of possible solutions.

All the models explain the observed travel time residuals to within about the measurement error. For example, model B diminishes the variance of the residuals by 60% leaving an unmodeled variance of 0.0036 $s^2/\%^2$, which compares favorably with the timing accuracy of about 0.05 s.

DISCUSSION

Inversion Model

The three-dimensional velocity structure obtained from the inversion reveals several significant features (Figure 5 and Plate 1*a*). (Plate 1 can be found in the separate color section in this issue.) The most important of these is the low-velocity anomaly in the middle crust under the southern part of the Mono Craters. Its top is about 8–10 km deep (depending on the inversion model). The feature is visible clearly in layers 3 and 4 of all models and may reach to the bottom of the crust in layer 5 ($\approx$32 km). Its slowest velocity is about 7% below the mean and occupies a single block in layer 3. Since damping in the inversion tends to reduce the magnitude of these velocity estimates, the velocity of the feature may be even lower. Because the array is 30 km in diameter, we do not have much information from depths greater than about 30 km and cannot determine whether the anomaly continues into the mantle.

Though this main low-velocity feature is relatively compact, it does appear to be somewhat asymmetric. In particular, the center shifts significantly between layers 3 and 4, suggesting an east dipping structure. This dip is apparent in the east-west cross section of Plate 1*a* and in similar cross sections (not shown) of a set of models with differing block arrangements. The easterly dip probably is not an artifact of the inversion since more west dipping than east dipping rays are used in the inversion. The resolution matrix (Figure 6*b*, discussed in the next section) confirms this interpretation. The observed dip suggests that the east dipping Sierran frontal fault zone or an eastward (outward) dipping zone of weakness associated with the mylonitized cataclastic border of a Cretaceous pluton beneath Pumice Valley [e.g., *Kistler*, 1966] may influence the location of the low-velocity anomaly.

In addition to this low-velocity anomaly, some smaller features are visible. A high-velocity region in the northwestern corner of the model lies beneath the Sierra (layers 1 and 2) and may be caused by high-velocity basement rock. Similar high-velocity features were observed by *Iyer et al.* [1981*a*, *b*] and *Evans* [1982] under the Idaho Batholith. A second high-velocity anomaly is centered near the south end of the Mono Craters in layers 1 and 2. It coincides with a magnetic low [*U.S. Geological Survey*, 1974] which may be caused by carbonate metasediments in Sierran roof pendant rocks (R. Bailey, personal communication, 1985). Such rocks crop out nearby and in other areas along a larger north-south magnetic low of which this one is a part. Where they appear nearby along the crest of the Sierra Nevada, these rocks have higher density than the neighboring granitic rocks [*Oliver*, 1977] and may therefore have higher seismic velocities than the granitic rocks which crop out west of the Mono Craters. The thickness of this roof pendant is uncertain but could be as great as 5 or 6 km, based on observed variations in hypocenter patterns with depth south of Long Valley (R. Cockerham, personal communication, 1985). Finally, a low-velocity feature appears beneath Mono basin in layers 1 and 2 and may continue to depth. Since it lies on the edge of the model and is poorly resolved (diagonal elements of $\mathbf{R} < 0.4$ or 0.5), its interpretation is uncertain. It may reflect deeper down-faulted material in Mono basin contrasting with faster surrounding granitic rocks, or strictly speaking, it even might be shallow magma beneath the northernmost Mono Craters. There is, however, no compelling reason to believe this feature is anything but an artifact of the inversion's modeling of the shallow sediments of Mono basin. Since there is abundant evidence for such sediments, we perfer not to overinterpret the data by looking too far for alternative, less probable sources.

Inversion Model Resolution

An examination of the model resolution helps in evaluating the significance of features seen in the inversion result. The resolution matrix calculated by the inversion is best understood by

$$\hat{m} = \mathbf{R}m \tag{7}$$

[e.g., *Ellsworth*, 1977], which relates the "true" model m to the inversion result $\hat{m}$. The "truth" of m, which ideally is the real earth structure, is limited largely by the model parameterization (i.e., the selection of block sizes and boundaries). Each element of the symmetric singular matrix $\mathbf{R}$ is between -1 and $+1$ (>0 on the diagonal) so that each row of the matrix is an averaging kernel relating all of m to one block in $\hat{m}$. That is, $\hat{m}$ is some average, hopefully local, of the parameterized real earth structure m.

Thus in most cases large diagonal elements in $\mathbf{R}$ indicate that the velocity estimates in $\hat{m}$ are dominated by velocities in the same regions in m, that is, that $\hat{m}$ is a good representation of m. Figures 6*a*–6*c* shows that the diagonal elements of $\mathbf{R}$ are ≥ 0.6 for most of the central parts of our models. Figure 6*b* and Plate 1*b* show the row of $\mathbf{R}$ for the block in model B believed to contain the most anomalous material. This row of $\mathbf{R}$ is typical of the blocks in this central part of the velocity model. The averaging kernel for this block is compact, so the velocity estimate probably is not strongly influenced by anomalies outside the block. Thus we believe that the models presented are well resolved on the block level and generally are interpretable if their velocity perturbations are significantly larger than the standard errors, which average about 0.8% (Figures 6*a*–6*c*).

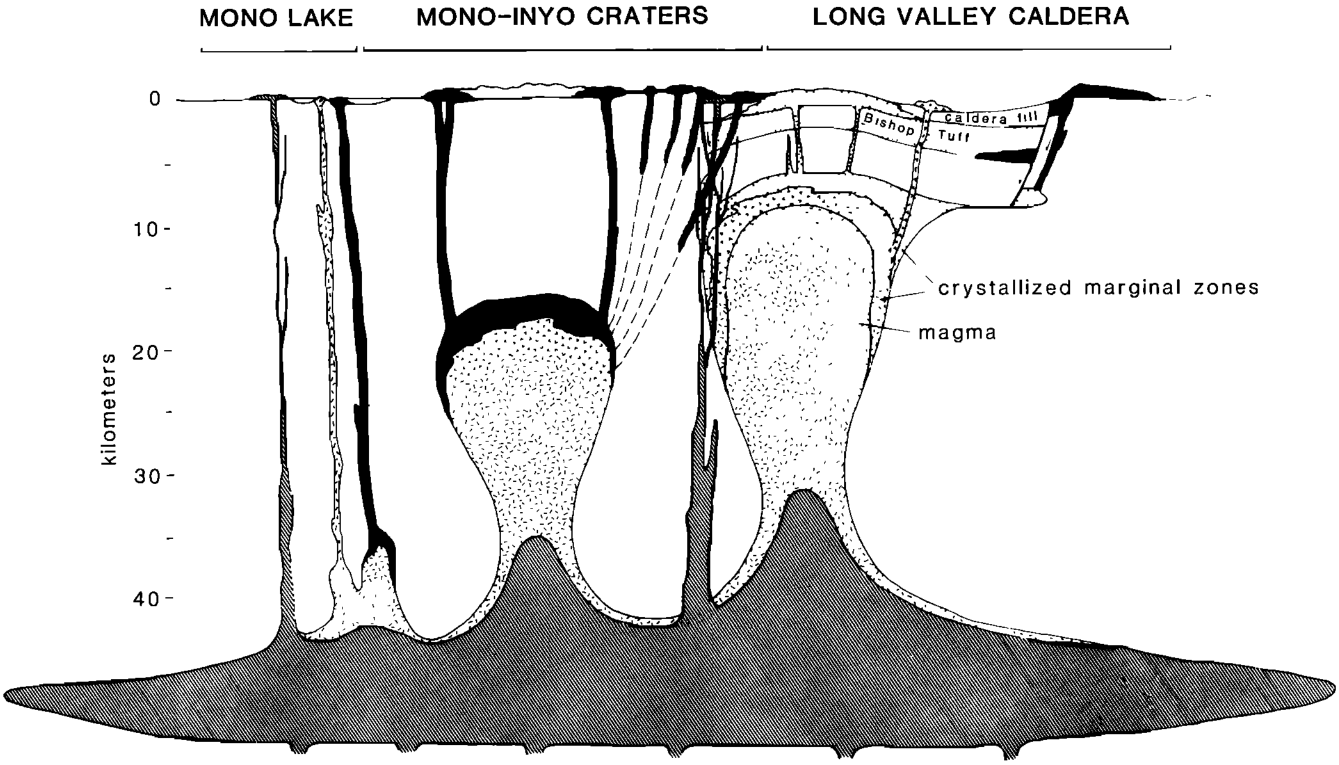

Fig. 7. Magmatic model of *Bailey* [1982], by permission.

The sediments filling Mono basin, on the other hand, form a relatively thin horizontal layer and are near the edge of the models. Because resolution is usually poor near the edges of models and because thin horizontal layers are parasitic cases and always are modeled badly by the "ACH" method, it is best to take a different approach to interpreting the resolution of this anomaly. Comparing the uncorrected (model A) and corrected (model B) cases (Figures 5*a*–5*e* and Figures 6*a* and 6*b*) one can see the strong influence of the first layer sediments on the second layer; deeper layers are less affected by this "smearing out" of the sediment velocity anomaly. In the corrected case the remaining perturbations in the first layer are only about 4%, compared with 12% for the uncorrected case. Nevertheless, the shape of the first-layer anomaly is similar in both cases, suggesting that the sediment corrections around Mono Lake should be larger than the ones used or, alternatively, that the second layer also may be slow under Mono Lake. The models' resolution of this feature is insufficient to discriminate between these possibilities.

The third layer, however, clearly is decoupled from these effects. There is no significant change in the pattern in layer 3 between the corrected and uncorrected cases. Similarly, layer 4 is very similar in all the models. Layer 5 differes in model C, presumably because of the greater depth of this layer in model C.

Interpretation

Bailey [1982] inferred from geological and geochemical arguments that the Mono Craters are fed by a shallow ring dike from an active midcrustal magma chamber. Even though it is somewhat smaller, shallower, and displaced eastward, we interpret the low-velocity anomaly beneath the Mono Craters as this chamber. Many rock properties can produce low velocities, but the location of this feature beneath a young, increasingly active volcanic chain and the observed and predicted velocity decreases due to melt and partial melt in crystalline materials [e.g., *Goetze*, 1977; *Mavko*, 1980] support this interpretation. Also, the intensity of the anomaly and its depth, similar to low-velocity anomalies found under other small young silicic centers, support our interpretation that the low velocities are caused by melt or partial melt [e.g., *Iyer*, 1984].

The bulk melt fraction present in the chamber is much more difficult to estimate. The gross distribution of melt in the chamber, the geometry of the melt fraction itself (whether it wets crystal faces, for example), the melt viscosity, and the relative importances of phase change, melt squirt, and other proposed attenuation mechanisms all are poorly known and all affect such estimates strongly. A low-viscosity melt wetting crystal faces could produce the observed velocity perturbation with on the order of 1% melt [e.g., *Mavko*, 1980]. On the other hand, the very low phenocryst content of erupted magmas suggests that at least part of the chamber may be as much as 100% melted (R. Bailey, personal communication, 1986).

Given such gross uncertainties, we propose only the following elementary estimate. The velocities of rhyolite melt [*Murase and McBirney*, 1973] and dacite melt [*Hayakawa et al.*, 1957] seem to be about 4 km/s, which would provide a 36% velocity contrast with country rock (6.25 km/s) if present in layer 3. If the velocities of the solid and melt part average in a simple volume-weighted fashion (they may well not), then the melt fraction to produce a 7% velocity anomaly would be of the order of 20%.

The volume of the chamber is somewhat difficult to estimate accurately because it is similar to the size of the blocks (about 200 km^3). The anomaly does appear to involve at least one full block, since it also seems to affect several blocks neighboring the most anomalous one. It does not appear to involve fully more than about three blocks. We conclude that the magma chamber is between about 200 and 600 km^3 in volume. This volume is less than that of the Bisho Tuff erupted from Long Valley [*Bailey*, 1982] and presumably is much smaller than the magma chamber that produced that tuff. Coupled with the youth of the Mono Craters, this relatively small magma chamber volume suggests that a major ash flow event is not now likely (e.g., R. Bailey, personal communication, 1985).

Bailey [1982] speculates that Long Valley and the Mono Craters may have a common mafic magmatic source in the mantle, which supplies heat to the individual shallower midcrustal silicic chambers (Figure 7). Our observations do not contradict this model; in fact, they tend to confirm at least the shallower part of it. However, they do suggest that the active fluid volume of magma is located more directly beneath the Mono Craters themselves, rather than beneath Pumice Valley, centered within the ring fracture zone.

Unfortunately, there are few other geophysical data to help constrain our Mono Craters model. The data reported by *Kissling et al.* [1984], who derived a tomographic model for depths of 0–14 km at Long Valley using local earthquake travel times, extend north to the Mono Craters, but resolution is poor in that area. This tomographic model shows moderately low-velocity material beneath the Mono Craters throughout the sampled depth range and is generally similar to the teleseismic result. However, the tomographic anomaly extends to shallower depth than the teleseismic anomaly. In particular, it shows low velocities from 3 to 9 km depth near the south end of the Mono Craters, whereas the teleseismic model, which appears to be well resolved in this area, shows faster than average velocities at these depths (Figure 5*b*). Closer examination of the stations and sources used by Kissling et al. suggests that the region may be sampled mostly by subparallel roughly north striking rays arriving at a station at the north end of the Mono Craters, near our station MD2. MD2 exhibits a 0.2-s sediment anomaly. Thus the tomographic model for this area partly may reflect an ill-resolved sediment anomaly and therefore may be less reliable locally than the teleseismic model. However, because of these differing results the presence of a high-velocity anomaly near the south end of the Mono Craters suggested by teleseismic data cannot be considered proven.

Other geophysical data are less applicable. Only one heat flow measurement [*Lachenbruch et al.*, 1976] is available for the Mono Craters area. It is west of the craters at Aeolian Buttes and has a normal Basin and Range value (91 mW m^{-2}) [*Lachenbruch et al.*, 1976; A. Lachenbruch, written communication, 1982]. A. Lachenbruch (personal communication, 1984) indicates that this result does not preclude the presence of a young magma chamber at depth, because if it is as young as it appears, heat flow from it should not have perturbed surface temperatures yet. For example, a magma chamber less than 700,000 years old and more than 10 km deep, or less than 150,000 years old and 6 km deep would not perturb surface temperatures significantly even directly above the chamber.

The gravity data are equally inconclusive. The regional Bouguer gravity map [*Oliver and Robbins*, 1978] shows a small 5-mGal low at the southern end of the Mono Craters, but the feature represents data from only one gravity station. A simple model (a 200 km^3 upright cylinder with its top 10 km beneath the Mono Craters, a diameter of 6 km, and a height of 7.5 km) would produce a 1.5-mGal anomaly if it had a density contrast of 0.2 g/cm^3. This gravity signature would be swamped by larger local features and might not be separable from uncertainties (which easily could exceed 3 mGal) in the Bouguer reduction density for the volcanic pile.

Finally, *Hermance et al.* [1984] report a magnetotelluric study in Pumice Valley. They did not observe a decrease in resistivity at shallow depths and concluded that the magma chamber for the Mono Craters is either too thin or too deep (> 10 km) to be resolved or is significantly displaced from the center of the ring fracture. Since the teleseismic results show that the low-velocity feature is 5–10 km east of Pumice Valley and below about 10 km depth, the magnetotelluric observations do not contradict our results.

CONCLUSIONS

The relative residual patterns obtained from teleseismic compressional wave arrivals recorded in the Mono Craters area imply the presence of a low-velocity feature under the southern part of the Mono Craters. Inversion of these data provides a moderate resolution three-dimensional velocity image of the feature. The velocity structure modeled predicts the observed travel time delays to within their expected reading errors. It reveals a small low-velocity anomaly in the middle crust mostly between about 10- and 20-km depth and with a maximum velocity decrease of about 7%. The low-velocity anomaly may continue to the Moho as an east dipping feature.

A proposed explanation for the feature is the presence of silicic melt or partial melt under the Mono Craters in a magma chamber partly controlled by the Sierran frontal fault zone or the mylonitic border zone of a Cretaceous pluton. This hypothesis is largely consistent with the geologic observations of Kistler and Bailey but does not support the notion of a larger midcrustal chamber centered beneath Pumice Valley and within the Mono Craters ring fracture zone (Figure 1). The volume of the interpreted magma chamber is greater than 200 km^3 but is substantially smaller than the chamber that existed under Long Valley before eruption of the 600 km^3 Bishop Tuff. The melt fraction in the Mono Craters magma chamber is poorly constrained by these teleseismic data but may be of the order of 20%.

APPENDIX

The "remaining variance" in Table 2*a* is, strictly speaking, only an estimate of the data variance left unexplained by the model $\hat{m}$. The equation used, however, can be derived from equations (5) and (6) with only the approximations already implicit in those equations and the assertion that the remaining variance is

$$\sigma r^2 = \frac{e^T e}{(N_{\text{obs}} - N_{\text{ev}})} \tag{A1}$$

where the error $e = d - \mathbf{A}\hat{m}$ and N_{obs} and N_{ev} are the number of observations and events, respectively (D. A. Stauber and D. Oppenheimer, personal communication, 1986). The sum square error is

$$(d - \mathbf{A}\hat{m})^T(d - \mathbf{A}\hat{m}) = d^T d - x^T\hat{m} - \hat{m}^T x + \hat{m}^T(\mathbf{G} - \theta^2\mathbf{I})\hat{m} \tag{A2}$$

where the solution $\hat{m}$ obeys equation (6) rewritten as

$$\hat{m} = \mathbf{G}^{-1}x \tag{A3}$$

with $\mathbf{G} = (\mathbf{A}^T\mathbf{A} + \theta^2\mathbf{I})$ and $x = \mathbf{A}^T d$. Since $x^T\hat{m} = \hat{m}^T x$, equation (A2) rearranges to

$$e^T e = d^T d - \hat{m}^T x - \hat{m}^T\theta^2\hat{m} + \hat{m}^T(\mathbf{G}\hat{m} - x) \tag{A4}$$

where equation (A3) implies that the last term vanishes. The inversion uses equations (A1) and (A4) to estimate the remaining variance, so this estimate is exact within the linearity assumptions in equation (5) and the assertion that the system has $N_{obs} - N_{ev}$ degrees of freedom.

Ellsworth [1977] compares the value σr^2 obtained from (A1) and (A4) with values obtained by raytracing through $\hat{m}$. He estimates that σr^2 leads to variance reduction estimates that are about 5% optimistic in complex models. Our conclusions in the text based on the variance reduction and σr^2 are not affected by differences of this magnitude.

Acknowledgments. We gratefully acknowledge the help of Richard Buszka, friend and colleague, much of whose last work is represented in the illustrations for this report. Richard died August 13, 1985, of injuries inflicted by a hit and run driver. We miss his special good humor and his skills. We would like to thank Roy Bailey, Rob Cockerham, Cliff Thurber, John Rundle, David Oppenheimer, and Doug Stauber for their reviews of the manuscript and their many useful suggestions. Moses Smith and John Coakley assisted in the field. This work was supported by the U.S. Geological Survey's Geothermal Research Program and by the Universitaet Fridericiana Karlsruhe (Special Research Project SFB 108).

REFERENCES

Aki, K., A. Christoffersson, and E. S. Husebye, Determination of the three-dimensional seismic structure of the lithosphere, *J. Geophys. Res., 82,* 237–296, 1977.

Aki, K., and W. H. K. Lee, Determination of three-dimensional velocity anomalies under a seismic array using first *P* arrival times from local earthquakes, 1, A homogeneous initial model, *J. Geophys. Res., 81,* 4381–4399, 1976.

Bailey, R. A., Other potential eruption centers in California: Long Valley, Mono Lake, Coso, and Clear Lake volcanic fields, *Calif. Div. Mines Geol. Spec. Publ., 63,* 17–28, 1982.

Bailey, R. A., and R. P. Koeppen, Preliminary geologic map of Long Valley caldera, Mono County, California, scale 1:62,500, *U.S. Geol. Surv. Open File Rep., 77-468,* 20 pp., 1977.

Bailey, R. A., G. B. Dalrymple, and M. A. Lanphere, Volcanism, structure and geochronology of Long Valley caldera, Mono County, California, *J. Geophys. Res., 81,* 725–744, 1976.

Criley, E., and J. Eaton, Five-day recorder seismic system, *U.S. Geol. Surv. Open File Rep., 78-266,* 85 pp., 1978.

Ellsworth, W. L., Three-dimensional structure of the crust and mantle beneath the Island of Hawaii, Ph.D. thesis, 377 pp., Mass Inst. of Technol., Cambridge, 1977.

Ellsworth, W. L., and R. Y. Koyanogi, Three-dimensional crust and mantle structure of Kilauea Volcano, Hawaii, *J. Geophys. Res., 82,* 5379–5394, 1977.

Evans, J. R., Compressional wave velocity structure of the upper 350 km under the eastern Snake River Plain near Rexburg, Idaho, *J. Geophys. Res., 87,* 2654–2670, 1982.

Franklin, J., Well posed stochastic extensions of ill-posed linear problems, *J. Math. Anal. Appl., 21,* 682–716, 1970.

Goetze, C., A brief summary of our present day understanding of the effect of volatiles and partial melt on the mechanical properties of the upper mantle, in *High Pressure Research: Applications in Geophysics,* edited by M. H. Manghuani and S. Akimoto, pp. 3–23, Academic, Orlando, Fla., 1977.

Hayakawa, M. et al., Prospecting of the underground structure at "Shōwa-Shinzan" by various geophysical methods, particularly seismic survey, *Jpn. J. Geophys., 1,* 13–20, 1957.

Hermance, J. F., W. M. Slocum, and G. A. Neumann, The Long Valley/Mono Basin volcanic complex: A preliminary magnetotelluric and magnetic variation interpretation, *J. Geophys. Res., 89,* 8325–8337, 1984.

Herrin, E., et al., 1968 seismological tables for *P*-phases, *Bull. Seismol. Soc. Am., 58,* 1193–1241, 1968.

Hill, D. P., Structure of Long Valley Caldera, California, from a seismic refraction experiment, *J. Geophys. Res., 81,* 745–753, 1976.

Iyer, H. M., Geophysical evidence for the locations, shapes and sizes, and internal structures of magma chambers beneath regions of Quaternary volcanism, *Philos. Trans. R. Soc. London, Ser. A, 310,* 473–510, 1984.

Iyer, H. M., and R. M. Stewart, Teleseismic technique to locate magma in the crust and upper mantle, Magma Genesis, Proceedings of the American Geophysical Union Chapman Conference on Partial Melting in the Earth's Upper Mantle, *Bull. Oreg. Dep. Geol. Miner. Ind., 96,* 281–299, 1977.

Iyer, H. M., D. H. Oppenheimer, and T. Hitchcock, Large scale teleseismic delays in the Geysers–Clear Lake geothermal area, California, *Science, 204,* 495–497, 1979.

Iyer, H. M., J. R. Evans, G. Zandt, R. M. Stewart, J. M. Coakley, and J. N. Roloff, A deep low-velocity body under the Yellowstone caldera, Wyoming: Delineation using teleseismic *P*-wave residuals and tectonic interpretation, part I, *Geol. Soc. Am. Bull., 92,* 792–798, 1981*a*.

Iyer, H. M., J. R. Evans, G. Zandt, R. M. Stewart, J. M. Coakley, and J. N. Roloff, A deep low-velocity body under the Yellowstone caldera, Wyoming: Delineation using teleseismic *P*-wave residuals and tectonic interpretation, part II, *Geol. Soc. Am. Bull., 92,* 1471–1646, 1981*b*.

Kissling, E., W. L. Ellsworth, and R. S. Cockerham, Three-dimensional structure of the Long Valley caldera, California, region by geotomography, vol. 1, *U.S. Geol. Surv. Open File Rep., 84-939,* 188–220, 1984.

Kistler, R. W., Structure and metamorphism in the Mono Craters quadrangle, Sierra Nevada, California, *U.S. Geol. Surv. Bull., 1221-E,* 53 pp., 1966.

Lachenbruch, A. H., J. H. Sass, R. J. Munroe, and T. H. Moses, Geothermal setting and simple heat conduction models for the Long Valley caldera, *J. Geophys. Res., 81,* 769–784, 1976.

Levenberg, K., A method for the solution to certain non-linear problems in least squares, *Q. Appl. Math., 2,* 164–168, 1944.

Mavko, G. M., Velocity and attenuation in partially molten rocks, *J. Geophys. Res., 85,* 5173–5189, 1980.

Murase, T. and A. R. McBirney, Properties of some common igneous rocks and their melts at high temperatures, *Geol. Soc. Am. Bull., 84,* 3563–3592, 1973.

Oliver, H. W., Gravity and magnetic investigations of the Sierra Nevada batholith, California, *Geol. Soc. Am. Bull., 88,* 445–461, 1977.

Oliver, H. W. and S. L. Robbins, Bouguer gravity map of California, Mariposa sheet, Calif. Div. of Mines and Geol., Sacramento, 1978.

Oppenheimer, D. H., and K. E. Herkenhoff, Velocity-density properties of the lithosphere from three-dimensional modeling at The Geysers–Clear Lake region, California, *J. Geophys. Res., 86,* 6057–6065, 1981.

Pakiser, L. C., Seismic exploration of Mono Basin, California, *J. Geophys. Res., 81,* 3607–3618, 1976.

Reasenberg, P., W. Ellsworth, and A. Walter, Teleseismic evidence for a low-velocity body under the Coso geothermal area, *J. Geophys. Res., 85,* 2471–2483, 1980.

Robinson, R., and H. M. Iyer, Delineation of a low-velocity body under the Roosevelt hot springs area, Utah, using teleseismic *P*-wave data, *Geophysics, 46,* 1456–1466, 1981.

Sharp, A. D. L., P. M. Davis, and F. Gray, A low velocity zone beneath Mount Etna and magma storage, *Nature, 287,* 587–591, 1980.

Steeples, D. W., and H. M. Iyer, Low-velocity zone under Long Valley as determined from teleseismic events, *J. Geophys. Res., 81,* 849–860, 1976.

Strand, R. G., Geologic map of California: Mariposa sheet (Olaf P. Jenkins edition), scale 1:250,000, Calif. Div. of Mines and Geol., Sacramento, 1967.

U.S. Geological Survey, Aeromagnetic map of parts of the Walker Lake and Mariposa 1° × 2° quadrangles, eastern California, scale 1:250,000, Open File Map, Menlo Park, Calif., 1974.

Waff, H. S., and J. R. Bulau, Equilibrium fluid distribution in an ultramafic partial melt under hydrostatic stress conditions, *J. Geophys. Res., 84,* 6109–6114, 1979.

U. Achauer, Geophysikalisches Institut, Universität Fridericiana Karlsruhe, Hertz Str. 16, Bar 42, Karlsruhe, D-7500, Federal Republic of Germany.

J. R. Evans, L. Greene, and H. M. Iyer, U.S. Geological Survey, 345 Middlefield Road, MS 977, Menlo Park, CA 94025.

(Received April 8, 1986;
revised June 24, 1986;
accepted July 30, 1986.)

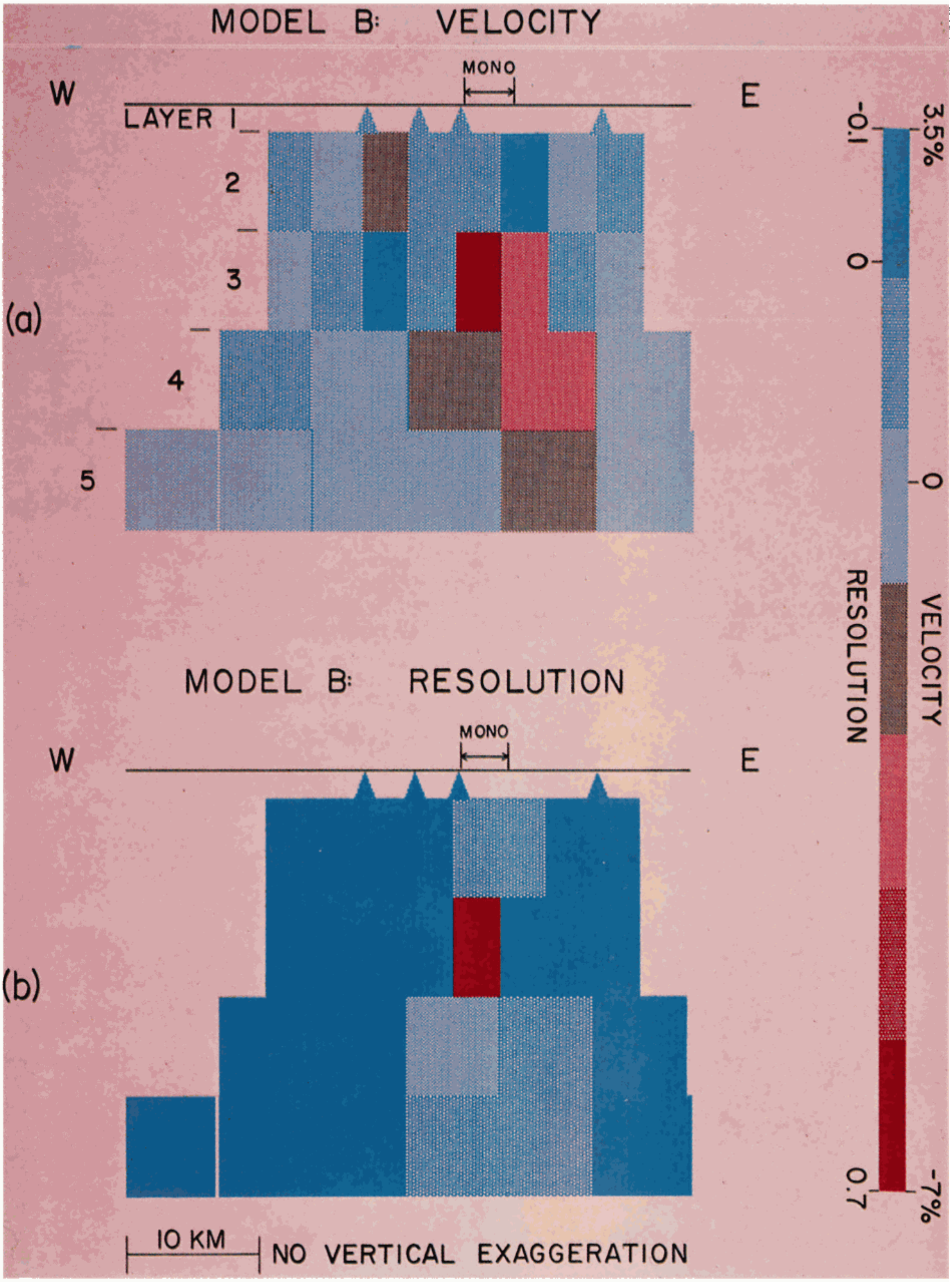

Plate 1 [*Achauer et al.*]. (*a*) Vertical cross section of model B along a line (Figure 5*c*) through the suspected magma chamber. Velocity perturbations are coded by color with low velocities in magenta. (*b*) The row of the resolution matrix corresponding to the most anomalous block in Plate 1*a*.